Microglia mediate synaptic plasticity induced by 10 Hz repetitive magnetic stimulation

Amelie Eichler[1], Dimitrios Kleidonas[1,2,3], Zsolt Turi[1], Matthias Kirsch[1], Dietmar Pfeifer[4], Takahiro Masuda[5,6], Marco Prinz[5,7,8], Maximilian Lenz[1,#], Andreas Vlachos[1,8,9,#]

[1]Department of Neuroanatomy, Institute of Anatomy and Cell Biology, Faculty of Medicine, University of Freiburg, Freiburg, Germany.

[2]Spemann Graduate School of Biology and Medicine, University of Freiburg, Freiburg, Germany.

[3]Faculty of Biology, University of Freiburg, Freiburg, Germany.

[4]Department of Hematology, Oncology and Stem Cell Transplantation, Medical Center, Faculty of Medicine, University of Freiburg, Freiburg, Germany.

[5]Institute of Neuropathology, Faculty of Medicine, University of Freiburg, Freiburg, Germany.

[6]Department of Molecular and System Pharmacology, Graduate School of Pharmaceutical Sciences, Kyushu University, Fukuoka 812-8582, Japan.

[7]Signalling Research Centres BIOSS and CIBSS, University of Freiburg, Freiburg, Germany.

[8]Center for Basics in Neuromodulation (NeuroModulBasics), Faculty of Medicine, University of Freiburg, Freiburg, Germany.

[9]Center Brain Links Brain Tools, University of Freiburg, Freiburg, Germany.

[#] joint senior authors

*Correspondence to:

Andreas Vlachos, M.D.
Department of Neuroanatomy
Institute of Anatomy and Cell Biology
Albert-Ludwigs-Universität Freiburg
Albertstr. 17
79104 Freiburg, Germany

Email: andreas.vlachos@anat.uni-freiburg.de

Keywords: microglia, synaptic plasticity, repetitive magnetic stimulation

ABSTRACT

Introduction: Repetitive transcranial magnetic stimulation (rTMS) is a non-invasive brain stimulation technique that is widely used in clinical practice for therapeutic purposes. Nevertheless, the mechanisms that mediate its therapeutic effects remain poorly understood. Recent work implicates that microglia, the resident immune cells of the central nervous system, have a defined role in the regulation of physiological brain function, e.g. the expression of synaptic plasticity. Despite this observation, no evidence exists for a role of microglia in excitatory synaptic plasticity induced by rTMS.

Methods: Here, we used repetitive magnetic stimulation of organotypic entorhino-hippocampal tissue cultures to test for the role of microglia in synaptic plasticity induced by 10 Hz repetitive magnetic stimulation (rMS). For this purpose, we performed PLX3397 (Pexidartinib) treatment to deplete microglia from tissue culture preparations. Using whole-cell patch-clamp recordings, live-cell microscopy, immunohistochemistry and transcriptome analysis, we assessed structural and functional properties of both CA1 pyramidal neurons and microglia to correlate the microglia phenotype to synaptic plasticity.

Results: PLX3397 treatment over 18 days reliably depletes microglia in tissue cultures, without affecting structural and functional properties of CA1 pyramidal neurons. Microglia-depleted cultures display defects in the ability of CA1 pyramidal neurons to express plasticity of excitatory synapses upon rMS. Notably, rMS induces a moderate release of proinflammatory and plasticity-promoting factors, while microglial morphology stays unaltered.

Conclusion: We conclude that microglia play a crucial role in rMS-induced excitatory synaptic plasticity.

INTRODUCTION

Despite its increasingly prevalent clinical use, the cellular and molecular effects of repetitive transcranial magnetic stimulation (rTMS) remain poorly understood (Cirillo et al., 2017; Muller-Dahlhaus and Vlachos, 2013). It is widely known, however, that the electric fields produced by magnetic stimulation modulate neural excitability and synaptic transmission in cortical circuits (Pell et al., 2011). These changes require neural activity, i.e., action potential induction, and Ca^{2+}-dependent signaling pathways, i.e., NMDA receptors and L-Type voltage-gated calcium channels (Lenz et al., 2015). They are consistent with a long-term potentiation (LTP) of synaptic neurotransmission (Vlachos et al., 2012). It remains unclear, though, how rTMS and the induction of "LTP-like" plasticity asserts positive effects in clinical settings.

Recent work suggests that microglia, the resident immune cells of the brain, sense and regulate synaptic transmission and plasticity (Badimon et al., 2020; Schafer et al., 2012). Evidence has been provided that changes in network activity modulate microglia states (Pfeiffer et al., 2016; Stowell et al., 2019). These changes are reflected by the dynamic extension and retraction of microglial processes, by the formation of physical contacts between microglia and neurons, and by the activity-dependent secretion of soluble microglial factors (Akiyoshi et al., 2018; Cserep et al., 2020; Sheppard et al., 2019). Specifically, the plasticity-promoting effects of pro-inflammatory cytokines, such as tumor necrosis factor alpha (TNFα) and Interleukin 6 (IL6), have been demonstrated in several experimental settings, both *in vitro* and *in vivo* (Heir and Stellwagen, 2020; Santello et al., 2011; Stellwagen and Malenka, 2006). These findings suggest that microglia play an important role in neural function and plasticity. Considering their role in pathological brain states (Graeber and Streit, 2010; Prinz et al., 2019; Prinz et al., 2021), it is interesting to speculate that the therapeutic effects of rTMS could—at least in part—depend on the modulation of microglia function. Indeed, experimental evidence has been provided that rTMS affects microglial markers (Clarke et al., 2017; Cullen and Young, 2016; Li et al., 2021;

Muri et al., 2020; Stevanovic et al., 2019). However, direct experimental evidence for a role of microglia in rTMS-induced plasticity is currently missing.

In our recent work we demonstrated concentration-dependent effects of TNFα on synaptic plasticity, where low concentrations of TNFα promoted plasticity induction, whereas high concentrations impeded the ability of neurons to express synaptic plasticity (Maggio and Vlachos, 2018). Consistent with these findings we were able to show that a pathological activation of microglia, as seen under conditions of bacterial infection and sepsis (Strehl et al., 2014), blocks the ability of neurons to express synaptic plasticity induced by 10 Hz repetitive magnetic stimulation (rMS; (Lenz et al., 2020)). We therefore theorized that the "physiological" (i.e., plasticity-inducing) effects of rMS depend on microglia. To address the biological relevance of microglia in rMS-induced synaptic plasticity, in this study we depleted microglia from organotypic brain tissue cultures and probed synaptic plasticity with 10 Hz rMS. In turn, we tested for the effects of 10 Hz rMS on the structural and functional properties of microglia, which have been recently shown to maintain their *in vivo* tissue imprints in three-week-old organotypic tissue cultures (Delbridge et al., 2020).

MATERIALS AND METHODS

Ethics statement. Mice were maintained in a 12 h light/dark cycle with food and water available *ad libitum*. Every effort was made to minimize distress and pain of animals. All experimental procedures were performed according to German animal welfare legislation and approved by the appropriate animal welfare committee and the animal welfare officer of Albert-Ludwigs-University Freiburg, Faculty of Medicine (X-17/07K, X-17/09C, X-18/02C).

Preparation of tissue cultures. Entorhino-hippocampal tissue cultures were prepared at postnatal day 3-5 from *C57BL/6J*, *HexB-tdTom* (Masuda et al., 2020), and *C57BL/6-Tg(TNFa-eGFP)* (Lenz et al., 2020) mice of either sex as previously described (Lenz et al., 2015). Cultivation medium contained 50% (v/v) MEM, 25% (v/v) basal medium eagle, 25% (v/v) heat-inactivated normal horse serum, 25 mM HEPES buffer solution, 0.15% (w/v) bicarbonate, 0.65% (w/v) glucose, 0.1 mg/ml streptomycin, 100 U/ml penicillin, and 2 mM glutamax. The pH was adjusted to 7.3. All tissue cultures were allowed to mature for at least 18 days in a humidified atmosphere with 5% CO_2 at 35°C. Cultivation medium was replaced 3 times per week.

Pharmacology. Tissue cultures were treated immediately after preparation (div 0) with PLX3397 (50 nM; #2501 Axon) for at least 18 days. Vehicle-only treated cultures (DMSO, 0.1 µl) served as age- and time-matched controls.

Repetitive magnetic stimulation *in vitro*. Tissue cultures (≥ 18 days *in vitro*) were transferred to a 35 mm Petri Dish filled with pre-warmed standard extracellular solution containing (in mM): 129 NaCl, 4 KCl, 1 $MgCl_2$, 2 $CaCl_2$, 4.2 glucose, 10 HEPES, 0.1 mg/ml streptomycin, 100 U/ml penicillin, pH 7.4 with NaOH, osmolarity adjusted with sucrose to 380-390 mOsm. Cultures were stimulated using the Magstim Rapid^2 stimulator (Magstim Company, UK) connected to a Double AirFilm® Coil (coil parameters according to manufacturer's description:

average inductance = 12 µH; pulse rise time approximately 80 µs; pulse duration = 0.5 ms, biphasic; Magstim Company, UK) with a biphasic current waveform. Cultures were positioned approximately 1 cm under the center of the coil and oriented in a way that the induced electric field was parallel to the dendritic tree of CA1 pyramidal neurons. The stimulation protocol consisted of 900 pulses at 10 Hz (50% maximum stimulator output). Cultures were kept in the incubator for at least 2 h after stimulation before experimental assessment. Age- and time-matched control cultures were not stimulated, but otherwise treated identical to stimulated cultures.

Propidium iodide staining. Tissue cultures were incubated with propidium iodide (PI, 5 µg/ml; #P3566 Invitrogen) for 2 h, washed in phosphate buffered saline (PBS) and fixed as described below. Cultures treated for 4 h with NMDA (50 µg/ml; #0114 Tocris) served as positive controls in these experiments. Cell nuclei were stained with DAPI, sections were mounted on microscope slides and confocal images were acquired as described below.

Immunostaining and imaging. Tissue cultures were fixed overnight in a solution of 4% (w/v) paraformaldehyde (PFA) in PBS (prepared from 16% PFA stocks in phosphate buffered saline according to manufacturer's instruction; #28908 Thermo Scientific). After fixation, cultures were washed in PBS (0.1 M, pH 7.4) and consecutively incubated for 1 h with 10% (v/v) normal goat serum (NGS) in 0.5% (v/v) Triton X-100 containing PBS to reduce nonspecific staining and increase antibody penetration. Subsequently, cultures were incubated overnight at 4°C with rabbit anti-Iba (1:1000; #019-19741 Fujifilm Wako) in PBS with 10% NGS and 0.1% Triton X-100. Sections were washed and incubated overnight at 4°C with appropriate Alexa Fluor® dye-conjugated secondary antibodies (1:1000, donkey anti-rabbit Alexa Fluor 488 or 647; #A-21206 or #A-32795 Invitrogen) in PBS with 10% NGS or NHS, 0.1% Triton X-100. For post-hoc visualization of patched pyramidal cells, Streptavidin Alexa Fluor 488 (Streptavidin A488, 1:1000; #S32354 Invitrogen) was added to the secondary antibody incubation solution. DAPI

nuclear stain (1:2000 in PBS for 20 minutes; #62248 Thermo Scientific) was used to visualize cytoarchitecture. Cultures were washed, transferred onto glass slides and mounted for visualization with DAKO anti-fading mounting medium (#S302380-2 Agilent).

A Leica SP8 laser-scanning microscope equipped with a 20x multi-immersion (NA 0.75; Leica), a 40x oil-immersion (NA 1.30; Leica) and a 63x oil-immersion objective (NA 1.40; Leica) was used for confocal image acquisition. Image stacks for analysis of microglia cell density (Figure 1) and images of propidium iodide stainings (Figure 3) were acquired with a 20x objective at 0.75x optical zoom (resolution: 512 x 512 px). Image stacks for spine density and spine volume analysis (Figure 6) were acquired with a 63x oil-immersion objective at 5.0x optical zoom (resolution: 1024 x 1024, $\Delta z = 0.22$ µm at ideal Nyquist rate). Image stacks of Iba1 stained *HexB-tdTom* cultures (Figure S1) were acquired with a 20x objective at 2.0x optical zoom (resolution: 512 x 512 px). Laser intensity and detector gain were set to achieve comparable overall fluorescence intensity throughout stacks between all groups in each experimental setting.

Live-cell imaging. Live-cell imaging of tissue cultures was performed at a Zeiss LSM800 microscope equipped with a 10x water-immersion (NA 0.3; Carl Zeiss) and a 40x water-immersion objective (NA 1.0; Carl Zeiss). Filter membranes with 2 to 6 cultures were placed in a 35 mm Petri Dish containing pre-oxygenated imaging solution consisting of 50% (v/v) MEM, 25% (v/v) basal medium eagle, 50 mM HEPES buffer solution (25% v/v), 0.65% (w/v) glucose, 0.15% (w/v) bicarbonate, 0.1 mg/ml streptomycin, 100 U/ml penicillin, 2 mM glutamax and 0.1 mM trolox. The cultures were kept at 35°C during the imaging procedure.

Live-cell imaging of homozygous (*HexB*$^{tdT/tdT}$) and heterozygous (*HexB*$^{tdT/+}$) cultures prepared from *HexB-tdTom* transgenic animals was performed to assess microglia morphology after rMS. Cultures were stimulated as described above (rMS and sham stimulation) and imaging was started immediately in imaging solution under continuous oxygenation (5% CO_2

/ 95% O_2). For 3 hours, every 2 minutes a z-stack of the same cell was recorded using a 40x water-immersion objective with $\Delta z = 1$ µm at ideal Nyquist rate and an optical zoom of 1.0x (resolution 512 x 512 px, 2x line average). Laser intensity and detector gain were initially set and were kept constant over image acquisition time.

Live-cell imaging of *C57BL/6-Tg(TNFa-eGFP)* cultures was performed to monitor TNFα expression after rMS as an indicator of neuroinflammation. Cultures were stimulated as described above (rMS and sham stimulation) and kept in the incubator after stimulation. After 3 hours a z-stack of each culture was recorded using a 10x water-immersion objective with $\Delta z = 6.3$ µm at ideal Nyquist rate and an optical zoom of 0.5x (resolution 1024 x 1024 px). Laser intensity and detector gain were initially set to keep the fluorescent signal in a dynamic range throughout the experiment and were kept constant.

Confocal image stacks were stored as .czi files.

Transcriptome Microarray. Tissue cultures that were cultivated on one filter membrane (3 cultures) were transferred as one sample into RLT buffer (QIAGEN) and RNA was isolated according to the manufacturer's instructions (RNeasy Plus Micro Kit; #74034 QIAGEN). RNA was eluted in 50 µl water and precipitated in 0.75 M ammonium-acetate and 10 µg glycogen (#R0551 Thermo Scientific) by adding 125 µl ethanol (100%). Samples were incubated at -80°C overnight and consecutively centrifuged for 30 minutes at 4°C. Pellets were washed with 70% ethanol, centrifuged again and dried. Finally, pellets were dissolved in water for further processing. RNA concentration and integrity was consecutively analyzed by capillary electrophoresis using a Fragment Analyser (Advanced Analytical Technologies, Inc., USA). RNA samples with RNA quality numbers (RQN) > 8.0 were further processed with the Affymetrix WT Plus kit and hybridized to Clariom S mouse arrays as described by the manufacturer (Thermo Fisher, Germany). Briefly, labeled fragments were hybridized to arrays for 16 h at 45°C, 60 rpm in a GeneChip™ Hybridization Oven (Thermo Fisher, Germany).

After washing and staining, the arrays were scanned with the Affymetrix GeneChip Scanner 3000 7G (Thermo Fisher, Germany). CEL files were produced from the raw data with Affymetrix GeneChip Command Console Software Version 4.1.2 (Thermo Fisher, Germany).

Cytokine detection assay. To analyze protein release upon rMS, cultures were stimulated on incubation medium in interface configuration with three cultures grown on one filter membrane. Three hours after stimulation, both incubation medium (for detection of protein release) and tissue cultures (for gene expression analysis) were collected and frozen in liquid nitrogen until further processing.

For cytokine detection, a V-Plex Proinflammatory Panel 1 (mouse) Kit Plus (#K15048G Mesoscale Discovery) was used. The collected incubation medium was diluted 1:1 in diluent provided with the kit. Protein detection was performed according to manufacturer's instructions. A pre-coated plate with capture antibodies on defined spots was incubated with the diluted samples for 2 h. After washing, samples were incubated for 2 h with a solution containing electrochemiluminescent MSD SULFO-TAG detection antibodies (Mesoscale Discovery; Antibodies: Anti-ms TNFα Antibody #D22QW, Anti-ms IL6 Antibody #D22QX, Anti-ms CXCL1 Antibody #D22QT). After washing, samples were measured with a MESO QuickPlex SQ 120 instrument (Mesoscale Discovery). The respective protein concentrations were determined using the MSD DISCOVERY WORKBENCH software (Mesoscale Discovery).

RNA Isolation and Quantitative reverse transcription PCR (RT-qPCR). RNA isolation for qPCR analysis was performed as follows. Tissue cultures that were cultivated on one filter membrane (3 cultures) were transferred as one sample into RNA Protection buffer (New England Biolabs) and RNA was isolated according to the manufacturer's instructions (Monarch® Total RNA Miniprep Kit; #T2010S New England Biolabs). As a quality control the RIN (RNA integrity number) value of each sample was determined. RIN analysis was

performed using the Agilent RNA 6000 Pico Kit (#5067-1513 Agilent) with a 2100 Bioanalyzer (#G2939BA Agilent). RIN Values are reported in supplementary table T2. Purified RNA was consecutively reverse transcribed (RevertAid RT Kit; #K1691 Thermo Scientific). cDNA was diluted in water to a final concentration of 3 ng/ml. RT-qPCR was performed using a C1000 Touch Thermal Cycler (BIO-RAD) and the CFX 384 Real-Time PCR system (BIO-RAD). 13.5 ng target cDNA diluted in TaqMan Gene Expression Master Mix (Applied Biosystems #4369016) were amplified using standard TaqMan gene expression assays (Applied Biosystems; Assay-IDs: *Gapdh*: Mm99999915_g1; *Tnf*: Mm00443258_m1; *Il6*: Mm00446190_m1; *Cxcl1*: Mm04207460_m1). The RT-qPCR protocol was performed as follows: 1 cycle of 50°C for 2 min, 1 cycle of 95°C for 10 min, 40 cycles of 95°C for 15 s and 60°C for 1 min. Of each sample three technical replicates were used and no amplification was detected in non-template controls. Amplification curves were excluded from further analysis if efficiency values were less than 90 or exceeded 110 according to automated calculation by the Bio-Rad CFX Maestro software package. Data were exported and stored on a computer as .pcrd-files.

Whole-cell patch-clamp recordings. Whole-cell patch-clamp recordings were carried out at 35°C (3-6 neurons per culture). The bath solution contained (in mM) 126 NaCl, 2.5 KCl, 26 $NaHCO_3$, 1.25 NaH_2PO_4, 2 $CaCl_2$, 2 $MgCl_2$, and 10 glucose (aCSF) and was oxygenated continuously (5% CO_2 / 95% O_2). Patch pipettes contained (in mM) 126 K-gluconate, 10 HEPES, 4 KCl, 4 ATP-Mg, 0.3 GTP-Na_2, 10 PO-Creatine, 0.3% (w/v) biocytin (pH 7.25 with KOH, 290 mOsm with sucrose), having a tip resistance of 4-6 MΩ. Pyramidal neurons were visually identified using a LN-Scope (Luigs & Neumann) equipped with an infrared dot-contrast and a 40x water-immersion objective (NA 0.8; Olympus). Spontaneous excitatory postsynaptic currents (sEPSCs) of CA1 pyramidal neurons were recorded in voltage-clamp mode at a holding potential of -60 mV. Series resistance was monitored before and after each

recording and recordings were discarded if the series resistance reached ≥ 30 MΩ. For mEPSC recordings, D-APV (10 µM; #ab120003 Abcam), (-)-Bicuculline-Methiodide (10 µM; #ab120108 Abcam) and TTX (0.5 µM; #18660-81-6 Biotrend) were added to the external solution. For recording of intrinsic cellular properties in current-clamp mode, pipette capacitance of 2.0 pF was corrected and series resistance was compensated using the automated bridge balance tool of the MultiClamp commander. I-V-curves were generated by injecting 1 s square pulse currents starting at -100 pA and increasing in 10 pA steps until +500 pA current injection was reached (sweep duration: 2 s).

Multi-scale modeling. A 3-dimensional mesh model was created with two compartments (i.e., bath solution and organotypic tissue culture) using the finite element method and the program Gmsh (4.8.4). Local mesh resolution was increased from 0.01 to 0.004 units in the CA1 region of the culture (i.e., region of interest; ROI), where neurons were placed. The final mesh consisted of 3.55×10^6 nodes and 2.11×10^7 tetrahedrons. The mean tetrahedron edge length was 5.6 µm in the ROI. The physical dimensions of the mesh model were adapted from the *in vitro* setting.

The coil-to-culture distance was kept at 10 mm and the coil was positioned above the culture. Electrical conductivities for the bath and culture were 1.654 S m^{-1} and 0.275 S m^{-1}, respectively. The rate of change of the coil current was set to 1.4 A μs^{-1} at 1% MSO and it was scaled up to 50% MSO. Macroscopic electric field simulations were performed using SimNIBS (3.2.4) and Matlab (2020b). A validated 70 mm MagStim figure-of-eight coil was used in all simulations.

For multi-scale modeling, we used the Neuron Modeling for TMS (NeMo-TMS) framework to study the biological responses of CA1 pyramidal neurons to biphasic single pulse TMS and rTMS (Shirinpour et al., 2021). Axonal morphology was adopted from an example

cell (Shirinpour et al., 2021). For all neurons, we implemented the generalized version of the Jarsky model (Shirinpour et al., 2021).

We extracted the membrane potentials and voltage-gated calcium 'influx' from the somatic and dendritic compartments (Shirinpour et al., 2021). We analyzed the number of action potentials, calcium spikes and their peak values. Simulations were run on a high performance computer in the state of Baden-Württemberg, Germany (bwHPC).

Quantification and statistics. For the analysis of microglia cell density and spine density, cells or spines were counted manually in maximum intensity projections of the confocal image stacks using the 'Cell Counter' plugin of Fiji image processing package (available at https://fiji.sc/; (Schindelin et al., 2012)).

Spine head volumes were assessed in the confocal image stacks using the Imaris x64 (version 9.5.0) software. The surface tool with the 'split touching object' option enabled was used to measure the volume of spine heads. Files were stored as .ims.

Confocal images of PI stained cultures were processed and analyzed using the Fiji image processing package. After background subtraction (rolling ball radius 50 px), images were binarized and PI positive particles were displayed and counted using the 'Analyze Particles' function. Values were normalized to the mean value of the control group.

Confocal image stacks of heterozygous *C57BL/6-Tg(TNFa-eGFP)* cultures were processed and analyzed as previously described (Lenz et al., 2020) using the Fiji image processing package. Mean fluorescence intensity of the culture area was normalized to the mean value of fluorescence intensity of the sham-stimulated cultures in the respective round.

Dendritic morphologies were assessed using the Neurolucida® 360 software (version 2020.1.1). Cells were semi-automatically reconstructed with the 'user guided tree reconstruction' function. Reconstructions were saved as .DAT files and analysis was performed in the Neurolucida Explorer (version 2019.2.1).

To analyze microglia morphology, confocal image stacks were processed and analyzed using the Fiji image processing package. Of each z-stack a maximum intensity projection was generated and binarized using the 'Trainable Weka Segmentation' plugin (Arganda-Carreras et al., 2017). The same classifier was applied to all images of the same microglia over the recorded 3 h. After removing outliers (radius = 2 px, threshold = 50), microglia scanning density and microglia domain of each image were manually assessed as previously described (Pfeiffer et al., 2016). Values were normalized to the mean.

Single cell recordings were analyzed off-line using Clampfit 11 of the pClamp11 software package (Molecular Devices). sEPSC and mEPSC properties were analyzed using the automated template search tool for event detection (Lenz et al., 2021). Input resistance was calculated for the injection of -100 pA current at a time frame of 200 ms with maximum distance to the Sag-current. Resting membrane potential was calculated as the mean baseline value. AP detection was performed using the input/output curve threshold search event detection tool, and the AP frequency was assessed upon the number of APs detected during the respective injection step.

Statistical evaluation of the multi-scale modeling was implemented in R (4.0.3; https://www.R-project.org/) and R Studio (1.3.1093; http://www.rstudio.com/) integrated development environment. We ran generalized linear mixed models (GLMM) with predictors TREATMENT (two levels: control, PLX3397) and COMPARTMENT (three levels: soma, apical and basal dendrites). GLMM allows modeling dependent variables from different distributions and model both fixed and random effects (Stroup, 2012). The null model contained the cell as random intercept, and we added each predictor and their interaction terms one-by-one to the subsequent models. The Bayesian information criterion (BIC) was used to compare the current model with the previous one. We selected the winning model if the ΔBIC was at least 10 units less than for the null or previous model.

Affymetrix GeneChip™ microarray data (CEL files) were analyzed using the Affymetrix Transcriptome Analysis Console (TAC version 4.0.2.15). Gene expression was considered significantly different when FDR p-value < 0.05 and fold change < -2 or > 2. Differentially expressed well-annotated genes were considered 'microglia-specific' (Figure 1) if they were part of highly specific microglia markers found by Chiu et al. (Chiu et al., 2013) and 'microglia-related' if there was literature found that showed expression of these genes in microglia. A full list of differentially expressed genes including predicted genes is provided in supplementary table 1.

RT-qPCR data were analyzed as previously described (Lenz et al., 2020) with the Bio-Rad CFX Maestro 1.0 software package using the ΔΔCq method with *Gapdh* as reference gene. Values were normalized to the mean value of the respective vehicle-treated control group.

Mesoscale cytokine detection assay was analyzed using the MSD DISCOVERY WORKBENCH 4.0 platform. mRNA/protein level correlations were visualized by a linear regression fit and analyzed using non-parametric Spearman's correlation coefficients (r).

Data were analyzed using GraphPad Prism 7 (GraphPad software, USA). Statistical comparisons were made using non-parametric tests, since normal distribution could not be assured. For column statistics Mann-Whitney test (to compare two groups), and Kruskal-Wallis-test followed by Dunn's multiple comparisons were used. For statistical comparison of XY-plots, we used an RM two-way ANOVA test (repeated measurements/analysis) with Sidak's multiple comparisons. p-values < 0.05 were considered a significant difference. In the text and figures, values represent mean ± standard error of the mean (s.e.m.). * $p < 0.05$, ** $p < 0.01$, *** $p < 0.001$ and not significant differences are indicated by 'ns'.

Digital Illustrations. Figures were prepared using Photoshop graphics software (Adobe, San Jose, CA, USA). Image brightness and contrast were adjusted.

RESULTS

Pharmacologic depletion of microglia in organotypic tissue cultures

Organotypic tissue cultures were treated with the colony stimulating factor 1 receptor (CSF1R) antagonist PLX3397, which readily depletes microglia (Coleman et al., 2020; Elmore et al., 2014). Tissue cultures containing the entorhinal cortex and the hippocampus were exposed to 50 nM PLX3397 for at least 18 days *in vitro*, starting immediately after tissue culture preparation (Figure 1). A robust and almost complete depletion of microglia (~ 96% reduction in cell density) was observed in the three-week old tissue cultures, as demonstrated by immunostainings for the microglial marker Iba1 (Figure 1B-D).

Successful depletion of microglia was also confirmed with RNA microarray analysis (Figure 1E-G). We observed a significant reduction of microglia-specific and -related genes in the PLX3397 treated group (Figure 1E, F). Specifically, gene sets characteristic of M0-, M1-, and M2-classified microglia (Jurga et al., 2020) were reduced in our tissue cultures (Figure 1G). In turn, no major changes in the expression of genes related to astrocytes, oligodendrocytes, and neurons, i.e., synaptic genes were observed following microglia depletion. We conclude from these findings that treatment with PLX3397 results in a robust and specific depletion of microglia in three-week-old organotypic tissue cultures.

CA1 pyramidal neurons in microglia-depleted tissue cultures do not express rMS-induced synaptic plasticity

Microglia-depleted tissue cultures and non-depleted control cultures were stimulated with a 10 Hz stimulation protocol, consisting of 900 pulses at 50% maximum stimulator output using a Magstim Rapid^2 stimulator equipped with an AirFilm® coil (Figure 2A). The distance from the coil and the orientation of the stimulated tissue within the electric field were kept constant in all experiments (Figure 2A, B). CA1 pyramidal neurons were patched and α-amino-3-hydroxy-5-methyl-4-isoxazolepropionic acid (AMPA) receptor mediated miniature excitatory

postsynaptic currents (mEPSCs) were recorded 2–4 h after stimulation (Figure 2C, D). Sham-stimulated controls were treated the same way, except for stimulation. In line with previous work (Lenz et al., 2020; Lenz et al., 2015; Vlachos et al., 2012), 10 Hz rMS induced a robust strengthening of excitatory synapses onto CA1 pyramidal neurons in control tissue cultures, as demonstrated by the increased mean mEPSC amplitude, half width, area, and frequency (Figure 2D, E). Conversely, no changes in mEPSCs were observed in microglia-depleted tissue cultures following rMS (Figure 2F-H). These results demonstrate that the presence of microglia is required for rMS-induced synaptic plasticity.

Microglia depletion does not affect cell viability

Neurotrophic and neuroprotective effects of microglia are well recognized in the field (e.g., (Freria et al., 2020; Jin et al., 2017)). Although no obvious signs of cell death were observed in our experiments and despite the fact that baseline mEPSC properties were comparable between the two groups (c.f., Figure 2E and H), we decided to err on the side of caution and tested for alterations in cell viability as a potential confounding factor of rMS-induced synaptic plasticity. In these experiments propidium iodide (PI) stainings were used to assess viability and cell death in our preparations (Figure 3; c.f., (Lenz et al., 2020)). PI is a cell-membrane impermeant fluorescent molecule that binds to DNA. Hence, PI can be used as a marker for membrane integrity when applied to living tissue. Tissue cultures treated with PLX3397 (50 nM) or vehicle-only controls were stained with PI, while NMDA treated tissue cultures (50 µM, 4 h) served as a positive control in these experiments (Figure 3A). The PI-signal was comparably low in three-week-old control cultures and age- and time-matched PLX3397 treated preparations, while a significant increase in PI-signal was detected in the NMDA treated group (Figure 3B). We conclude from these results that the inability of CA1 pyramidal neurons to express rMS-induced synaptic plasticity is not based on changes in cell viability and cell death in the absence of microglia.

No major functional and structural changes of CA1 pyramidal neurons in microglia-depleted tissue cultures

Neuronal excitability and morphology are expected to have a major impact on the outcome of electromagnetic stimulation (Aberra et al., 2020; Shirinpour et al., 2021). Therefore, we tested for the effect of microglia depletion on structural and functional properties of CA1 pyramidal neurons in our experiments (Figure 4-6). Another set of CA1 pyramidal neurons was recorded in control and microglia-depleted tissue cultures and stained posthoc for morphological analysis (Figure 4A; c.f., Figures 5 and 6).

PLX3397-mediated microglia depletion did not affect the basic functional properties of CA1 pyramidal neurons, i.e., resting membrane potential (Figure 4B) and input resistance (Figure 4C). A slight but not significant difference in action potential frequency was observed for high current injections between the two groups (Figure 4D). Likewise, spontaneous EPSC amplitudes and frequencies were not significantly different between the groups (Figure 4E). We conclude from these results that depletion of microglia does not affect basic functional properties and synaptic activity of CA1 pyramidal neurons.

Consistent with these findings, sholl analysis of reconstructions of apical and basal dendrites did not show any major effects of microglia depletion on dendritic morphologies of CA1 pyramidal neurons (Figure 5A, B). We did not observe any significant differences in total dendritic length (Figure 5C), the number of branching points (Figure 5D), or the number of endpoints (Figure 5E).

Finally, a detailed morphological analysis of CA1 dendritic spines (Figure 6) confirmed our sEPSC recordings by demonstrating no significant differences in spine densities and spine head volumes between the two groups in CA1 stratum radiatum (Figure 6A), stratum oriens (Figure 6B) and stratum lacunosum-moleculare (Figure 6C). Taken together, we conclude that microglia depletion does not cause major structural and functional changes in CA1 pyramidal

neurons that could readily explain the inability of neurons to express rMS-induced synaptic plasticity in the absence of microglia.

Realistic multi-scale computer modeling predicts no major differences in rMS-induced depolarization and intracellular Ca^{2+} levels

We further evaluated the effects of 10 Hz rMS on CA1 pyramidal neurons using multi-scale computational modeling, to link the physical input parameters of rMS to dendritic morphologies and subcellular neural effects (Figure 7; (Shirinpour et al., 2021)). The reconstructed morphologies from recorded CA1 pyramidal neurons in microglia-depleted and non-depleted tissue cultures (c.f., Figure 5) were used in these experiments (Figure 7A). Both membrane voltage and calcium concentrations were assessed in this modeling approach (Figure 7B-F). We estimated the minimum synaptic weight that was just below the firing threshold of the CA1 pyramidal neurons. The synaptic weights of the model were not different in CA1 pyramidal neurons from depleted and non-depleted tissue cultures (Figure 7D).

We compared the peak spike values for the membrane voltage. The winning model ($\Delta BIC = 341.24$; $F_{2,102} = 1387.59$, $p = 2.2 \times 10^{-16}$) consisted of the compartment as predictor. Confirming our expectations, the analysis revealed significantly weaker peak values in the apical ($t = -48.524$, $p = 2.2 \times 10^{-16}$) and basal dendrites ($t = -6.563$, $p = 2.23 \times 10^{-9}$). However, the treatment had no effect on both the number of spikes (Figure 7D) and the peak action potential values in all compartments (Figure 7E).

We continued by comparing the peak calcium concentration values extracted from the compartments and treatment conditions. As for the voltage data, the winning model ($\Delta BIC = 189.3875$; $F_{2,102} = 283.51$, $p = 2.2 \times 10^{-16}$) consisted of the compartment as predictor. Again, the analysis revealed significantly weaker peak values in the apical ($t = -21.64$, $p = 2.2 \times 10^{-16}$) and basal dendrites ($t = -19.75$, $p = 2.2 \times 10^{-16}$). However, the treatment had no major effects on the peak calcium concentration levels in the investigated compartments (Figure 7F).

Repetitive magnetic stimulation does not affect structural properties of microglia

After demonstrating that structural and functional differences of CA1 pyramidal neurons do not explain our major findings (i.e., the inability of neurons to express rMS-induced synaptic plasticity in the absence of microglia), we considered the possible effects of rMS on the structural and functional (Figure 8, 9) properties of microglia.

To test for the effects of 10 Hz rMS on microglia morphology and dynamics, tissue cultures were prepared from the recently established transgenic *HexB-tdTom* mouse line, which expresses the red fluorescent protein tdTomato under the control of the Hexoaminidase B promotor (HexB) (Masuda et al., 2020). 97% of all tdTomato expressing cells also showed Iba1 staining, while in 98% of all Iba1 positive cells also tdTomato signal was detected (Figure S1). Apparently, the vast majority of microglia are readily identified in three-week-old tissue cultures prepared from *HexB-tdTom* mice.

We next employed live-cell microscopy and imaged microglia (i.e., tdTomato expressing cells) in CA1 stratum radiatum. Confocal image stacks were obtained every 2 minutes for 3 hours immediately after 10 Hz rMS or sham stimulation (Figure 8). In these experiments, we did not observe any major rMS-related changes in microglia morphologies. A detailed analysis of microglia dynamics in maximum intensity projections (Figure 8A-C) revealed no significant changes in dynamic microglial domains and microglial scanning densities between rMS-stimulated and sham-stimulated tissue cultures (Figure 8D). We conclude from these results that 10 Hz rMS does not lead to major changes in microglia morphology and dynamics.

Repetitive magnetic stimulation triggers TNFα and IL6 release

We then wondered whether 10 Hz rMS triggers an activation of microglia in the absence of major changes in microglia morphology. The plasticity modulating effects of secreted microglial factors are well-established (Cao et al., 2014; Chai et al., 2019; Habbas et al., 2015;

Heir and Stellwagen, 2020; Lenz et al., 2020; Maggio and Vlachos, 2018; Santello et al., 2011; Stellwagen and Malenka, 2006; Tancredi et al., 2000). Specifically, microglial TNFα, Il6 and Il1b have been linked to the ability of neurons to express synaptic plasticity (Lenz et al., 2020; Rizzo et al., 2018; Stellwagen and Malenka, 2006; Tancredi et al., 2000). In this context, we were recently able to demonstrate that low concentrations of TNFα promote the ability of neurons to express synaptic plasticity (Maggio and Vlachos, 2018). Therefore, we theorized that 10 Hz rMS could trigger the production and/or secretion of TNFα at low (i.e, plasticity-promoting) concentrations in our experimental setting.

qPCR-analyses and protein detection assays were performed in another set of rMS-stimulated and sham-stimulated tissue cultures (Figure 9A-C). Indeed, 10 Hz rMS triggered an increase in TNFα, both at the mRNA and protein level (Figure 9A). Moreover, a considerable increase in IL6 and CXCL1 also both at the mRNA and protein levels was detected (Figure 9B, C), while IL1β protein levels were below the detection threshold. These results support the notion that rMS leads to a functional activation of microglia, which promotes the ability of neurons to express rMS-induced synaptic plasticity.

Finally, we prepared tissue cultures from a transgenic TNFα reporter mouse line, which expresses the enhanced green fluorescent protein under the control of the TNF-promoter (*C57BL/6-Tg(TNFa-eGFP)*). Previously, we used this approach to demonstrate a pathological activation of microglia in the presence of bacterial lipopolysaccharides, which occludes the ability of neurons to express synaptic plasticity (Lenz et al., 2020). Live-cell microscopy revealed no obvious changes in eGFP fluorescence following 10 Hz rMS (Figure 9D), which is in line with a production and release of plasticity-promoting low concentrations of TNFα. Taken together, these results suggest that 10 Hz rMS induces a moderate increase/release in microglial cytokines (e.g., TNFα and IL6 (but not IL1b)), which contribute to the plasticity-promoting effects of 10 Hz rMS.

DISCUSSION

The experiments of this study demonstrate the involvement of microglia in rMS-induced synaptic plasticity: the presence of microglia is required for the induction of synaptic plasticity triggered by 10 Hz rMS. In this context, a robust functional activation of microglia is observed as reflected by changes in the expression of immune mediator gene sets and the release of TNFα and IL6 (but not IL1b). Interestingly, these changes occurred in the absence of major morphological changes of microglia and the dynamics of microglia were not affected by 10 Hz rMS. Considering the plasticity-promoting effects of microglial cytokines (Heir and Stellwagen, 2020; Maggio and Vlachos, 2018), we propose that the presence and functional activation of microglia is an important step in rTMS-induced synaptic plasticity.

During recent years experimental evidence has suggested that rTMS-induced after-effects are mediated by "LTP-like" plasticity mechanisms (Ziemann, 2004). This evidence is based on physiological characteristics and pharmacological analogies between studies performed at the system level in human subjects (Brown et al., 2020; Korchounov and Ziemann, 2011; Ziemann et al., 2015) and data obtained from animal models (Hoogendam et al., 2010; Vlachos et al., 2012). Specifically, the effects of pharmacological modulation of NMDA receptors have been interpreted as evidence for "LTP-like" plasticity, considering the relevance of NMDA receptors in LTP-induction (Brown et al., 2020; Lenz et al., 2015; Vlachos et al., 2012). Our own previous work demonstrated that pharmacological inhibition of NMDA receptors or L-Type voltage-gated calcium channels blocks the ability of neurons to express synaptic plasticity induced by 10 Hz rMS (Lenz et al., 2015; Vlachos et al., 2012). Consistent with these findings, stimulation in Ca^{2+}-free external solution failed to induce synaptic plasticity, thus confirming the relevance of Ca^{2+}-dependent signaling pathways in rMS-induced synaptic plasticity (Lenz et al., 2015). Notably, NMDA receptors and L-Type voltage-gated calcium channels are also expressed on microglia (Hopp, 2021; Murugan et al., 2011). In fact,

robust experimental evidence exists which demonstrates that modulation of intracellular Ca^{2+} levels regulate important microglia functions (Laprell et al., 2021). Hence, it is interesting to theorize that some of the results obtained in animal models and human studies could be explained—at least in part—by differential regulation of calcium signaling in microglia. Also, additional work is required to clarify whether rMS acts on microglia directly or whether microglia are activated indirectly by sensing rMS-induced changes in neuronal activity, e.g., via microglial glutamate receptors, purinergic receptors, or other signaling pathways (Cserep et al., 2020).

Regardless of these considerations, the experiments of the present study demonstrate that the presence of microglia is required for rMS-induced synaptic plasticity: CA1 pyramidal neurons in microglia-depleted tissue cultures did not express rMS-induced excitatory synaptic plasticity. These findings support the recently emphasized impact of glial cells in the neural effects of non-invasive brain stimulation (Gellner et al., 2021). Interestingly, we did not observe any obvious signs of functional and structural alterations of CA1 pyramidal neurons in microglia-depleted tissue cultures. Consistent with these findings multi-scale compartmental modeling confirmed that basic morphological and functional properties of neurons do not explain the inability of CA1 pyramidal neurons to express rMS-induced plasticity. We must concede, however, that detailed morphological reconstructions of axons were not obtained, as it is difficult to reliably visualize and reconstruct entire axon morphologies of individual neurons. Indeed, computational studies emphasize the relevance of axons and myelination in rTMS-induced synaptic plasticity (Aberra et al., 2020; Fields, 2005; Shirinpour et al., 2021; Wang et al., 2018). It should be noted, though, that we did not observe any differences in network activity in our experimental setting, as both sEPSC amplitudes and frequencies were not affected in microglia-depleted tissue cultures. Consistent with these findings we did not observe any differences in dendritic spine counts, and no evidence for alterations in oligodendrocyte markers was obtained in our RNA microarray analysis of microglia-depleted

tissue cultures. It is thus unlikely that major changes in the structural and functional properties of CA1 pyramidal neurons explain our results.

10 Hz rMS induced a robust increase in immune mediator gene sets and increased TNFα and IL6 production, suggesting that rMS activates microglia. Previous studies have demonstrated that proinflammatory cytokines influence excitatory neurotransmission (Cao et al., 2014; Maggio and Vlachos, 2018; Riazi et al., 2015; Sheppard et al., 2019; Stellwagen and Malenka, 2006; Strehl et al., 2014). Specifically, TNFα has been implicated as one of the secreted factors that modulate synaptic plasticity (Heir and Stellwagen, 2020). In this context it has been shown that TNFα acts as a permissive factor (Becker et al., 2013; Steinmetz and Turrigiano, 2010), where TNFα *per se* does not trigger changes in synaptic strength; rather, it modulates the ability of neurons to express plasticity without affecting baseline synaptic transmission. Indeed, experiments employing classic tetanic electric stimulation showed that low concentrations of TNFα promote LTP-induction, while high concentrations of TNFα impede the ability of neurons to express LTP (Maggio and Vlachos, 2018). These findings are consistent with metaplastic effects of TNFα. In line with this suggestion, pathological activation of microglia with bacterial lipopolysaccharides, which triggers strong TNFα production (i.e., ~10–15 fold increase in TNFα-mRNA and ~2000 fold increase in TNFα protein levels), occludes the ability of CA1 pyramidal neurons to express 10 Hz rMS-induced synaptic plasticity (Lenz et al., 2020). Together with the results of the present study, these findings demonstrate an important role of microglia in rTMS-induced synaptic plasticity. They call for a systematic assessment of rTMS-induced microglia plasticity, and raise the intriguing possibility that rTMS recruits metaplasticity by activating microglia (directly or indirectly). Hence, some of the beneficial effects of rTMS seen in patients may reside—at least in part—in the effects of rTMS on microglia function, which seem to also be involved in promoting the ability of neurons to express "LTP-like" plasticity shortly after rMS.

REFERENCES

Aberra, A.S., Wang, B., Grill, W.M., and Peterchev, A.V. (2020). Simulation of transcranial magnetic stimulation in head model with morphologically-realistic cortical neurons. Brain Stimul *13*, 175-189.

Akiyoshi, R., Wake, H., Kato, D., Horiuchi, H., Ono, R., Ikegami, A., Haruwaka, K., Omori, T., Tachibana, Y., Moorhouse, A.J., *et al.* (2018). Microglia Enhance Synapse Activity to Promote Local Network Synchronization. eNeuro *5*.

Arganda-Carreras, I., Kaynig, V., Rueden, C., Eliceiri, K.W., Schindelin, J., Cardona, A., and Sebastian Seung, H. (2017). Trainable Weka Segmentation: a machine learning tool for microscopy pixel classification. Bioinformatics *33*, 2424-2426.

Badimon, A., Strasburger, H.J., Ayata, P., Chen, X., Nair, A., Ikegami, A., Hwang, P., Chan, A.T., Graves, S.M., Uweru, J.O., *et al.* (2020). Negative feedback control of neuronal activity by microglia. Nature *586*, 417-423.

Becker, D., Zahn, N., Deller, T., and Vlachos, A. (2013). Tumor necrosis factor alpha maintains denervation-induced homeostatic synaptic plasticity of mouse dentate granule cells. Front Cell Neurosci *7*, 257.

Brown, J.C., DeVries, W.H., Korte, J.E., Sahlem, G.L., Bonilha, L., Short, E.B., and George, M.S. (2020). NMDA receptor partial agonist, d-cycloserine, enhances 10 Hz rTMS-induced motor plasticity, suggesting long-term potentiation (LTP) as underlying mechanism. Brain Stimul *13*, 530-532.

Cao, D.L., Zhang, Z.J., Xie, R.G., Jiang, B.C., Ji, R.R., and Gao, Y.J. (2014). Chemokine CXCL1 enhances inflammatory pain and increases NMDA receptor activity and COX-2 expression in spinal cord neurons via activation of CXCR2. Exp Neurol *261*, 328-336.

Chai, H.H., Fu, X.C., Ma, L., Sun, H.T., Chen, G.Z., Song, M.Y., Chen, W.X., Chen, Y.S., Tan, M.X., Guo, Y.W., *et al.* (2019). The chemokine CXCL1 and its receptor CXCR2 contribute to chronic stress-induced depression in mice. FASEB J *33*, 8853-8864.

Chiu, I.M., Morimoto, E.T., Goodarzi, H., Liao, J.T., O'Keeffe, S., Phatnani, H.P., Muratet, M., Carroll, M.C., Levy, S., Tavazoie, S., *et al.* (2013). A neurodegeneration-specific gene-expression signature of acutely isolated microglia from an amyotrophic lateral sclerosis mouse model. Cell Rep *4*, 385-401.

Cirillo, G., Di Pino, G., Capone, F., Ranieri, F., Florio, L., Todisco, V., Tedeschi, G., Funke, K., and Di Lazzaro, V. (2017). Neurobiological after-effects of non-invasive brain stimulation. Brain Stimul *10*, 1-18.

Clarke, D., Penrose, M.A., Harvey, A.R., Rodger, J., and Bates, K.A. (2017). Low intensity rTMS has sex-dependent effects on the local response of glia following a penetrating cortical stab injury. Exp Neurol *295*, 233-242.

Coleman, L.G., Jr., Zou, J., and Crews, F.T. (2020). Microglial depletion and repopulation in brain slice culture normalizes sensitized proinflammatory signaling. J Neuroinflammation *17*, 27.

Cserep, C., Posfai, B., Lenart, N., Fekete, R., Laszlo, Z.I., Lele, Z., Orsolits, B., Molnar, G., Heindl, S., Schwarcz, A.D., *et al.* (2020). Microglia monitor and protect neuronal function through specialized somatic purinergic junctions. Science *367*, 528-537.

Cullen, C.L., and Young, K.M. (2016). How Does Transcranial Magnetic Stimulation Influence Glial Cells in the Central Nervous System? Front Neural Circuits *10*, 26.

Elmore, M.R., Najafi, A.R., Koike, M.A., Dagher, N.N., Spangenberg, E.E., Rice, R.A., Kitazawa, M., Matusow, B., Nguyen, H., West, B.L., *et al.* (2014). Colony-stimulating factor 1 receptor signaling is necessary for microglia viability, unmasking a microglia progenitor cell in the adult brain. Neuron *82*, 380-397.

Fields, R.D. (2005). Myelination: an overlooked mechanism of synaptic plasticity? Neuroscientist *11*, 528-531.

Freria, C.M., Brennan, F.H., Sweet, D.R., Guan, Z., Hall, J.C., Kigerl, K.A., Nemeth, D.P., Liu, X., Lacroix, S., Quan, N., *et al.* (2020). Serial Systemic Injections of Endotoxin (LPS) Elicit Neuroprotective Spinal Cord Microglia through IL-1-Dependent Cross Talk with Endothelial Cells. J Neurosci *40*, 9103-9120.

Gellner, A.K., Reis, J., Fiebich, B.L., and Fritsch, B. (2021). Electrified microglia: Impact of direct current stimulation on diverse properties of the most versatile brain cell. Brain Stimul *14*, 1248-1258.

Graeber, M.B., and Streit, W.J. (2010). Microglia: biology and pathology. Acta Neuropathol *119*, 89-105.

Habbas, S., Santello, M., Becker, D., Stubbe, H., Zappia, G., Liaudet, N., Klaus, F.R., Kollias, G., Fontana, A., Pryce, C.R., *et al.* (2015). Neuroinflammatory TNFalpha Impairs Memory via Astrocyte Signaling. Cell *163*, 1730-1741.

Heir, R., and Stellwagen, D. (2020). TNF-Mediated Homeostatic Synaptic Plasticity: From in vitro to in vivo Models. Front Cell Neurosci *14*, 565841.

Hoogendam, J.M., Ramakers, G.M., and Di Lazzaro, V. (2010). Physiology of repetitive transcranial magnetic stimulation of the human brain. Brain Stimul *3*, 95-118.

Hopp, S.C. (2021). Targeting microglia L-type voltage-dependent calcium channels for the treatment of central nervous system disorders. J Neurosci Res *99*, 141-162.

Jin, W.N., Shi, S.X., Li, Z., Li, M., Wood, K., Gonzales, R.J., and Liu, Q. (2017). Depletion of microglia exacerbates postischemic inflammation and brain injury. J Cereb Blood Flow Metab *37*, 2224-2236.

Jurga, A.M., Paleczna, M., and Kuter, K.Z. (2020). Overview of General and Discriminating Markers of Differential Microglia Phenotypes. Front Cell Neurosci *14*, 198.

Korchounov, A., and Ziemann, U. (2011). Neuromodulatory neurotransmitters influence LTP-like plasticity in human cortex: a pharmaco-TMS study. Neuropsychopharmacology *36*, 1894-1902.

Laprell, L., Schulze, C., Brehme, M.L., and Oertner, T.G. (2021). The role of microglia membrane potential in chemotaxis. J Neuroinflammation *18*, 21.

Lenz, M., Eichler, A., Kruse, P., Strehl, A., Rodriguez-Rozada, S., Goren, I., Yogev, N., Frank, S., Waisman, A., Deller, T., *et al.* (2020). Interleukin 10 Restores Lipopolysaccharide-Induced Alterations in Synaptic Plasticity Probed by Repetitive Magnetic Stimulation. Front Immunol *11*, 614509.

Lenz, M., Kruse, P., Eichler, A., Straehle, J., Beck, J., Deller, T., and Vlachos, A. (2021). All-trans retinoic acid induces synaptic plasticity in human cortical neurons. Elife *10*.

Lenz, M., Platschek, S., Priesemann, V., Becker, D., Willems, L.M., Ziemann, U., Deller, T., Muller-Dahlhaus, F., Jedlicka, P., and Vlachos, A. (2015). Repetitive magnetic stimulation induces plasticity of excitatory postsynapses on proximal dendrites of cultured mouse CA1 pyramidal neurons. Brain Struct Funct *220*, 3323-3337.

Li, K., Wang, X., Jiang, Y., Zhang, X., Liu, Z., Yin, T., and Yang, Z. (2021). Early intervention attenuates synaptic plasticity impairment and neuroinflammation in 5xFAD mice. J Psychiatr Res *136*, 204-216.

Maggio, N., and Vlachos, A. (2018). Tumor necrosis factor (TNF) modulates synaptic plasticity in a concentration-dependent manner through intracellular calcium stores. J Mol Med (Berl) *96*, 1039-1047.

Masuda, T., Amann, L., Sankowski, R., Staszewski, O., Lenz, M., P, D.E., Snaidero, N., Costa Jordao, M.J., Bottcher, C., Kierdorf, K., *et al.* (2020). Novel Hexb-based tools for studying microglia in the CNS. Nat Immunol *21*, 802-815.

Muller-Dahlhaus, F., and Vlachos, A. (2013). Unraveling the cellular and molecular mechanisms of repetitive magnetic stimulation. Front Mol Neurosci *6*, 50.

Muri, L., Oberhansli, S., Buri, M., Le, N.D., Grandgirard, D., Bruggmann, R., Muri, R.M., and Leib, S.L. (2020). Repetitive transcranial magnetic stimulation activates glial cells and inhibits neurogenesis after pneumococcal meningitis. PLoS One *15*, e0232863.

Murugan, M., Sivakumar, V., Lu, J., Ling, E.A., and Kaur, C. (2011). Expression of N-methyl D-aspartate receptor subunits in amoeboid microglia mediates production of nitric oxide via NF-kappaB signaling pathway and oligodendrocyte cell death in hypoxic postnatal rats. Glia *59*, 521-539.

Pell, G.S., Roth, Y., and Zangen, A. (2011). Modulation of cortical excitability induced by repetitive transcranial magnetic stimulation: influence of timing and geometrical parameters and underlying mechanisms. Prog Neurobiol *93*, 59-98.

Pfeiffer, T., Avignone, E., and Nagerl, U.V. (2016). Induction of hippocampal long-term potentiation increases the morphological dynamics of microglial processes and prolongs their contacts with dendritic spines. Sci Rep *6*, 32422.

Prinz, M., Jung, S., and Priller, J. (2019). Microglia Biology: One Century of Evolving Concepts. Cell *179*, 292-311.

Prinz, M., Masuda, T., Wheeler, M.A., and Quintana, F.J. (2021). Microglia and Central Nervous System-Associated Macrophages-From Origin to Disease Modulation. Annu Rev Immunol *39*, 251-277.

Riazi, K., Galic, M.A., Kentner, A.C., Reid, A.Y., Sharkey, K.A., and Pittman, Q.J. (2015). Microglia-dependent alteration of glutamatergic synaptic transmission and plasticity in the hippocampus during peripheral inflammation. J Neurosci *35*, 4942-4952.

Rizzo, F.R., Musella, A., De Vito, F., Fresegna, D., Bullitta, S., Vanni, V., Guadalupi, L., Stampanoni Bassi, M., Buttari, F., Mandolesi, G., *et al.* (2018). Tumor Necrosis Factor and Interleukin-1beta Modulate Synaptic Plasticity during Neuroinflammation. Neural Plast *2018*, 8430123.

Santello, M., Bezzi, P., and Volterra, A. (2011). TNFalpha controls glutamatergic gliotransmission in the hippocampal dentate gyrus. Neuron *69*, 988-1001.

Schafer, D.P., Lehrman, E.K., Kautzman, A.G., Koyama, R., Mardinly, A.R., Yamasaki, R., Ransohoff, R.M., Greenberg, M.E., Barres, B.A., and Stevens, B. (2012). Microglia sculpt postnatal neural circuits in an activity and complement-dependent manner. Neuron *74*, 691-705.

Schindelin, J., Arganda-Carreras, I., Frise, E., Kaynig, V., Longair, M., Pietzsch, T., Preibisch, S., Rueden, C., Saalfeld, S., Schmid, B., *et al.* (2012). Fiji: an open-source platform for biological-image analysis. Nat Methods *9*, 676-682.

Sheppard, O., Coleman, M.P., and Durrant, C.S. (2019). Lipopolysaccharide-induced neuroinflammation induces presynaptic disruption through a direct action on brain tissue involving microglia-derived interleukin 1 beta. J Neuroinflammation *16*, 106.

Shirinpour, S., Hananeia, N., Rosado, J., Tran, H., Galanis, C., Vlachos, A., Jedlicka, P., Queisser, G., and Opitz, A. (2021). Multi-scale modeling toolbox for single neuron and subcellular activity under Transcranial Magnetic Stimulation. Brain Stimul.

Steinmetz, C.C., and Turrigiano, G.G. (2010). Tumor necrosis factor-alpha signaling maintains the ability of cortical synapses to express synaptic scaling. J Neurosci *30*, 14685-14690.

Stellwagen, D., and Malenka, R.C. (2006). Synaptic scaling mediated by glial TNF-alpha. Nature *440*, 1054-1059.

Stevanovic, I., Mancic, B., Ilic, T., Milosavljevic, P., Lavrnja, I., Stojanovic, I., and Ninkovic, M. (2019). Theta burst stimulation influence the expression of BDNF in the spinal cord on the experimental autoimmune encephalomyelitis. Folia Neuropathol *57*, 129-145.

Stowell, R.D., Sipe, G.O., Dawes, R.P., Batchelor, H.N., Lordy, K.A., Whitelaw, B.S., Stoessel, M.B., Bidlack, J.M., Brown, E., Sur, M., *et al.* (2019). Noradrenergic signaling in the wakeful state inhibits microglial surveillance and synaptic plasticity in the mouse visual cortex. Nat Neurosci *22*, 1782-1792.

Strehl, A., Lenz, M., Itsekson-Hayosh, Z., Becker, D., Chapman, J., Deller, T., Maggio, N., and Vlachos, A. (2014). Systemic inflammation is associated with a reduction in Synaptopodin expression in the mouse hippocampus. Exp Neurol *261*, 230-235.

Stroup, W.W. (2012). Generalized Linear Mixed Models: Modern Concepts, Methods and Applications. CRC Press.

Tancredi, V., D'Antuono, M., Cafe, C., Giovedi, S., Bue, M.C., D'Arcangelo, G., Onofri, F., and Benfenati, F. (2000). The inhibitory effects of interleukin-6 on synaptic plasticity in the rat hippocampus are associated with an inhibition of mitogen-activated protein kinase ERK. J Neurochem *75*, 634-643.

Vlachos, A., Muller-Dahlhaus, F., Rosskopp, J., Lenz, M., Ziemann, U., and Deller, T. (2012). Repetitive magnetic stimulation induces functional and structural plasticity of excitatory postsynapses in mouse organotypic hippocampal slice cultures. J Neurosci *32*, 17514-17523.

Wang, B., Grill, W.M., and Peterchev, A.V. (2018). Coupling Magnetically Induced Electric Fields to Neurons: Longitudinal and Transverse Activation. Biophys J *115*, 95-107.

Ziemann, U. (2004). TMS induced plasticity in human cortex. Rev Neurosci *15*, 253-266.

Ziemann, U., Reis, J., Schwenkreis, P., Rosanova, M., Strafella, A., Badawy, R., and Muller-Dahlhaus, F. (2015). TMS and drugs revisited 2014. Clin Neurophysiol *126*, 1847-1868.

DECLARATIONS

Acknowledgements: We thank Simone Zenker for skillful technical assistance and the Next Generation Sequencing Core Facility (NGS-CF, Faculty of Medicine, University of Freiburg) for assistance in transcriptome analysis. The authors also acknowledge the support by the state of Baden-Württemberg through the possibility of using high performance computing ressources (bwHPC; bwUniCluster 2.0). This work was supported by MOTI-VATE graduate school, Faculty of Medicine, University of Freiburg (to AE), the EQUIP Medical Scientist Programme, Faculty of Medicine, University of Freiburg (to ML), Faculty of Medicine of the University of Freiburg (TUR217/21; to ZT), and Deutsche Forschungsgemeinschaft (DFG; CRC/TRR 167–Project-ID B14; to AV).

Author Contributions: Author contributions have been assigned according to CRediT taxonomy. AE: Validation, Formal Analysis, Investigation, Writing-original draft preparation, Visualization, Funding acquisition. DK: Investigation. ZT: Investigation, Formal Analysis. MK: Investigation, Formal Analysis. DP: Resources. TM: Resources. MP: Resources. ML: Conceptualization, Methodology, Validation, Formal Analysis, Investigation, Writing-original draft preparation, Visualization, Supervision, Project administration, Funding acquisition. AV: Conceptualization, Methodology, Resources, Writing-original draft preparation, Supervision, Project administration, Funding acquisition.

Competing financial interests: The authors declare no competing interests.

FIGURE LEGENDS

Figure 1: PLX3397 depletes microglia in organotypic tissue cultures.

(A) Entorhino-hippocampal tissue culture stained with DAPI nuclear stain (EC, entorhinal cortex; DG, dentate gyrus). Scale bar, 200 µm.

(B, C) Representative examples of tissue cultures stained for the microglial marker Iba1. Note homogenous distribution of microglia in the control culture and almost complete depletion of microglia following PLX3397 treatment (50 nM, 18 days). Scale bars, 200 µm.

(D) Microglia cell counts in the respective groups ($n_{control}$ = 14 cultures, $n_{PLX(50nM)}$ = 15 cultures; Mann-Whitney test, U = 0).

(E-G) Affymetrix® Microarray analysis of control cultures and cultures treated with PLX3397. (E) Volcano plot shows fold changes and FDR p-values of analyzed transcripts. Significantly upregulated transcripts are indicated in green, significantly downregulated transcripts are indicated in red. (F) Classification of differentially expressed transcripts. 97.5% of the differentially expressed transcripts are microglia-specific or microglia-related. (G) Hierarchical clustering of differentially expressed gene sets characteristic of M0-, M1-, and M2-classified microglia. Each sample consisted of 3 pooled cultures (n = 3 samples in each group).

Individual data points are indicated by colored dots. Values represent mean ± s.e.m (***p < 0.001).

Figure 2: CA1 pyramidal neurons in microglia-depleted tissue cultures do not express excitatory synaptic plasticity induced by 10 Hz repetitive magnetic stimulation (rMS).

(A, B) Entorhino-hippocampal tissue cultures were stimulated with a 70 mm outer wing diameter figure of eight coil (Magstim Company, UK). Filter inserts carrying 2–6 tissue cultures were placed in a Petri Dish below the coil. The orientation within the electromagnetic field and distance to the coil was kept constant in all experiments (DAPI nuclear stain). Scale bar, 200 µm.

(C) Example of a recorded and posthoc stained CA1 pyramidal neuron in a tissue culture stained with the microglial marker Iba1. Scale bar, 100 µm.

(D, E) Sample traces and group data of AMPA receptor-mediated miniature excitatory postsynaptic currents (mEPSCs) recorded from CA1 pyramidal neurons in sham-stimulated and 10 Hz rMS-stimulated cultures 2 – 4 h after stimulation ($n_{control\text{-}sham}$ = 56 cells, $n_{control\text{-}rMS}$ = 60 cells; Mann-Whitney test, $U_{amplitude}$ = 1091, $U_{half\ width}$ = 1042, U_{area} = 956, $U_{frequency}$ = 651).

(F) Example of a recorded and posthoc stained CA1 pyramidal neuron in a PLX3397 treated, microglia-depleted tissue culture. Scale bar, 100 µm.

(G, H) Representative traces and group data of AMPA receptor-mediated mEPSCs recorded from CA1 pyramidal cells in sham-stimulated and 10 Hz rMS-stimulated microglia-depleted tissue cultures 2 – 4 h after stimulation ($n_{PLX3397\text{-}sham}$ = 61 cells, $n_{PLX3397\text{-}rMS}$ = 55 cells; Mann-Whitney test).

Individual data points are indicated by grey dots. Values represent mean ± s.e.m (** $p < 0.01$, *** $p < 0.001$; ns, not significant differences).

Figure 3: Depletion of microglia does not affect cell viability.

(A) Examples of vehicle-only controls, PLX3397 (50 nM, 18 d) and NMDA (50 µM, 4 h) treated tissue cultures stained with propidium iodide. Scale bars, 200 µm.

(B) Group data of quantified propidium iodide signals in the respective groups ($n_{control}$ = 29 cultures, $n_{PLX(50nM)}$ = 28 cultures, n_{NMDA} = 16 cultures; Kruskal-Wallis-test followed by Dunn's post-hoc correction).

Individual data points are indicated by grey dots. Values represent mean ± s.e.m (***$p < 0.001$; ns, not significant differences).

Figure 4: Basic functional properties of CA1 pyramidal neurons are not altered in microglia-depleted tissue cultures.

(A) Examples of patched, recorded and posthoc identified CA1 pyramidal neurons. Scale bar, 100 µm.

(B, C) Group data of passive membrane properties of CA1 pyramidal neurons in microglia-depleted, i.e., PLX3397 (50 nM, 18 days) treated tissue cultures and control cultures ($n_{control}$ = 33 cells, $n_{PLX3397}$= 30 cells; Mann-Whitney test).

(D) Group data of action potential frequencies of CA1 pyramidal neurons in the respective groups ($n_{control}$ = 33 cells, $n_{PLX3397}$ = 30 cells, RM two-way ANOVA followed by Sidak's multiple comparisons).

(E) Group data of AMPA receptor-mediated spontaneous excitatory postsynaptic currents (sEPSCs) recorded from CA1 pyramidal neurons revealed no significant changes in excitatory neurotransmission in microglia-depleted tissue cultures ($n_{control}$ = 33 cells, $n_{PLX3397}$ = 30 cells; Mann-Whitney test).

Individual data points are indicated by grey dots. Values represent mean ± s.e.m (ns, not significant differences).

Figure 5: Dendritic morphology of CA1 pyramidal cells is not affected in microglia-depleted tissue cultures.

(A) Examples of three dimensionally reconstructed CA1 pyramidal neurons in non-depleted controls and PLX3397 treated, i.e., microglia-depleted tissue cultures. Scale bars, 100 µm.

(B) Sholl analysis of apical and basal dendrites from reconstructed CA1 neurons in the respective groups ($n_{control}$ = 20 cells, $n_{PLX3397}$ = 15 cells; RM two-way ANOVA followed by Sidak's multiple comparisons).

(C-E) Group data of additional morphological parameters from the same set of reconstructed CA1 pyramidal neurons in microglia-depleted tissue cultures and vehicle-only treated control cultures ($n_{control}$ = 20 cells, $n_{PLX3397}$ = 15 cells; Mann-Whitney test).

Individual data points are indicated by grey dots. Values represent mean ± s.e.m (ns, not significant differences).

Figure 6: Dendritic spines of CA1 pyramidal neurons are not altered in microglia-depleted tissue cultures.

(A-C) Examples of dendritic segments and group data of spine densities and spine volumes from patched and posthoc identified CA1 pyramidal neurons in stratum radiatum (rad, A), stratum oriens (sor, B) and stratum lacunosum-moleculare (lcm, C) of PLX3397 treated, i.e., microglia-depleted tissue cultures and control cultures (rad density: $n_{control}$ = 16 dendritic segments, $n_{PLX3397}$ = 12 dendritic segments; rad volume: $n_{control}$ = 578 spines, $n_{PLX3397}$ = 393 spines; oriens density: $n_{control}$ = 15 dendritic segments, $n_{PLX3397}$ = 16 dendritic segments; oriens volume: $n_{control}$ = 450 spines, $n_{PLX3397}$ = 703 spines; lcm density: $n_{control}$ = 36 dendritic segments, $n_{PLX3397}$ = 23 dendritic segments; lcm volume: $n_{control}$ = 655 spines, $n_{PLX3397}$ = 405 spines; Mann-Whitney test). Scale bars, 3 µm.

Individual data points are indicated by grey dots. Values represent mean ± s.e.m (ns, not significant differences).

Figure 7: Multi-scale computer modeling of repetitive magnetic stimulation (rMS).

(A) Neuronal responses to rMS were modeled in realistic dendritic morphologies from reconstructed CA1 pyramidal neurons in a stereotypic tissue culture environment. EC, entorhinal cortex; DG, dentate gyrus. Scale bar, 200 µm.

(B, C) Changes in membrane voltage (Vm; B) and intracellular calcium levels (Ca^{2+}; C) were assessed for a train of 20 pulses at 10 Hz at the constant stimulation intensity used in the experimental setting. CA1 pyramidal neurons in both conditions showed a delayed suprathreshold response upon repetitive magnetic stimulation.

(D) Both the number of cellular spikes upon stimulation and the synaptic weight did not show a significant difference between CA1 pyramidal neurons from microglia-depleted and non-depleted control cultures ($n_{vehicle\text{-}only}$ = 20 cells, $n_{PLX3397}$ = 15 cells; GLMM).

(E) In the same set of cells the peak membrane voltage difference in response to magnetic stimulation was modeled in the somatic, apical and basal dendritic compartments. No differences were observed between the two groups, respectively.

(F) Analysis of stimulus-triggered changes in intracellular calcium levels. No changes in both the dendritic and the somatic compartments were evident between CA1 pyramidal neurons of microglia-depleted tissue cultures and control cultures.

Individual data points are indicated by grey dots. Values represent mean ± s.e.m. (ns, not significant difference).

Figure 8: Repetitive magnetic stimulation (rMS) does not affect microglia morphology.

(A-C) Examples of tdTomato expressing microglia in hippocampal area CA1 imaged from *HexB*$^{tdT/tdT}$ cultures over a period of three hours following 10 Hz rMS (2 min intervals). Maximum intensity projections of image-stacks (A), microglial scanning densities (B), and microglial domains (C) are illustrated. Scale bars, 15 µm.

(D) Group data of microglial domains and scanning densities from rMS-stimulated and sham-stimulated tissue cultures (n_{sham} = 6 cells, n_{rMS} = 6 cells from 6 cultures in each group; RM two-way ANOVA followed by Sidak's multiple comparisons).

Values represent mean ± s.e.m. (ns, not significant difference).

Figure 9: Repetitive magnetic stimulation (rMS) triggers the expression and release of plasticity-promoting microglial factors.

(A-C) Group data and correlation of mRNA and protein levels of (A) tumor necrosis factor alpha (TNFα), (B) interleukin 6 (IL6) and (C) chemokine ligand 1 (CXCL1) in 10 Hz rMS-stimulated tissue cultures and sham-stimulated controls. (n = 6 cultures or culturing medium samples respectively for each experimental condition; Mann-Whitney test, $U_{Tnf\ mRNA} = 2$, $U_{TNF\ protein} = 2$, $U_{Il6\ mRNA} = 2$, $U_{IL6\ protein} = 2$, $U_{Cxcl1\ mRNA} = 3$, $U_{CXCL1\ protein} = 0$, linear regression fit indicated by black line; Spearman's r in the figure panels).

(D) Sample images and group data of eGFP fluorescence intensity of rMS-stimulated and sham-stimulated tissue cultures prepared from TNF-reporter mice (*C57BL/6-Tg(TNFa-eGFP)*) imaged 3 h after 10 Hz rMS (DG, dentate gyrus; $n_{sham} = 26$ cultures, $n_{rMS} = 27$ cultures; Mann-Whitney test). Scale bars, 200 µm.

Individual data points are indicated by grey dots. Values represent mean ± s.e.m. (* $p < 0.05$, ** $p < 0.01$, *** $p < 0.001$; ns, not significant difference).

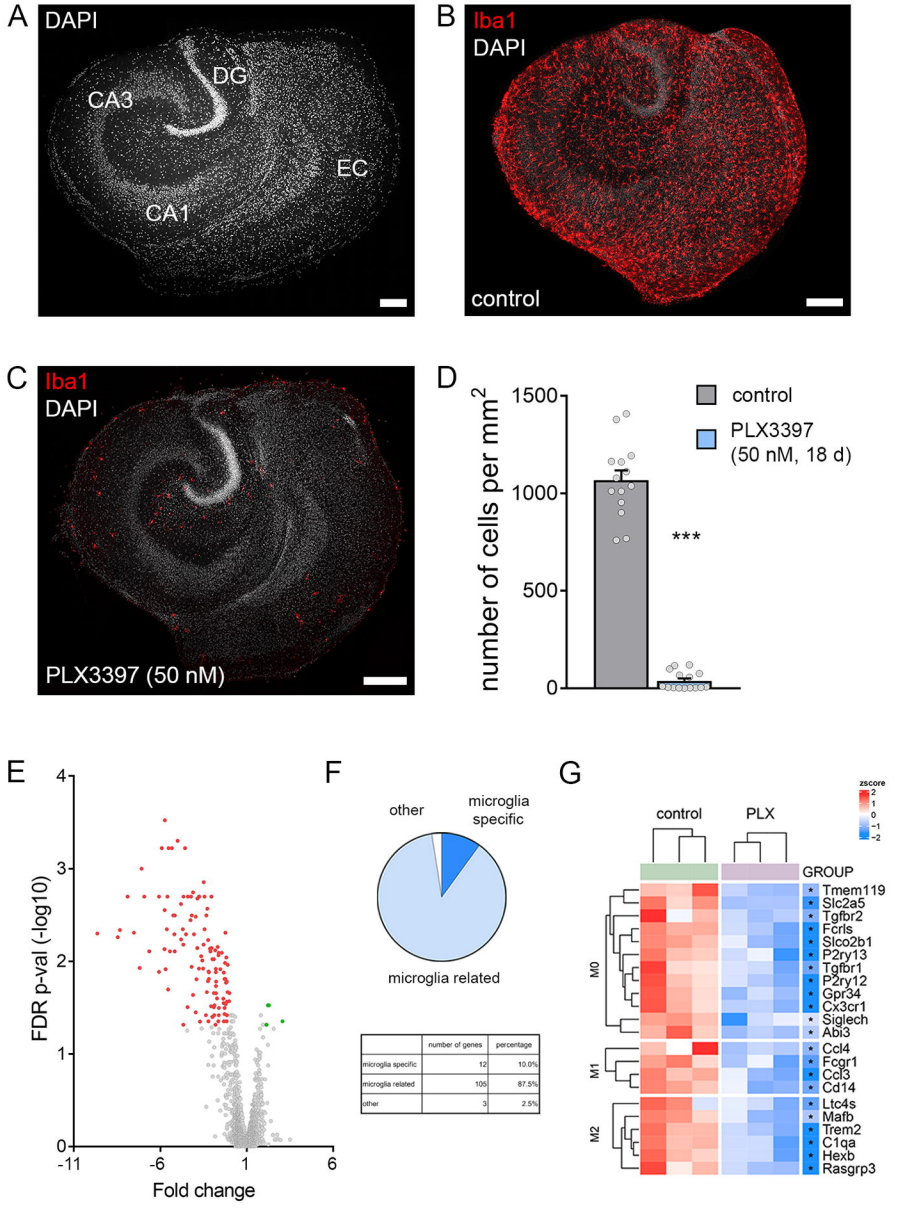
A
DAPI
DG
CA3
EC
CA1
B
Iba1
DAPI
control
C
Iba1
DAPI
PLX3397 (50 nM)
D
number of cells per mm2
1500
1000
500
0
control
PLX3397
(50 nM, 18 d)
***
E
FDR p-val (-log10)
4
3
2
1
0
-11
-6
1
6
Fold change
F
other
microglia
specific
microglia related
number of genes
percentage
microglia specific
12
10.0%
microglia related
105
87.5%
other
3
2.5%
G
zscore
2
1
0
−1
−2
control
PLX
GROUP
M0
M1
M2
Tmem119
Slc2a5
Tgfbr2
Fcrls
Slco2b1
P2ry13
Tgfbr1
P2ry12
Gpr34
Cx3cr1
Siglech
Abi3
Ccl4
Fcgr1
Ccl3
Cd14
Ltc4s
Mafb
Trem2
C1qa
Hexb
Rasgrp3

Figure 1

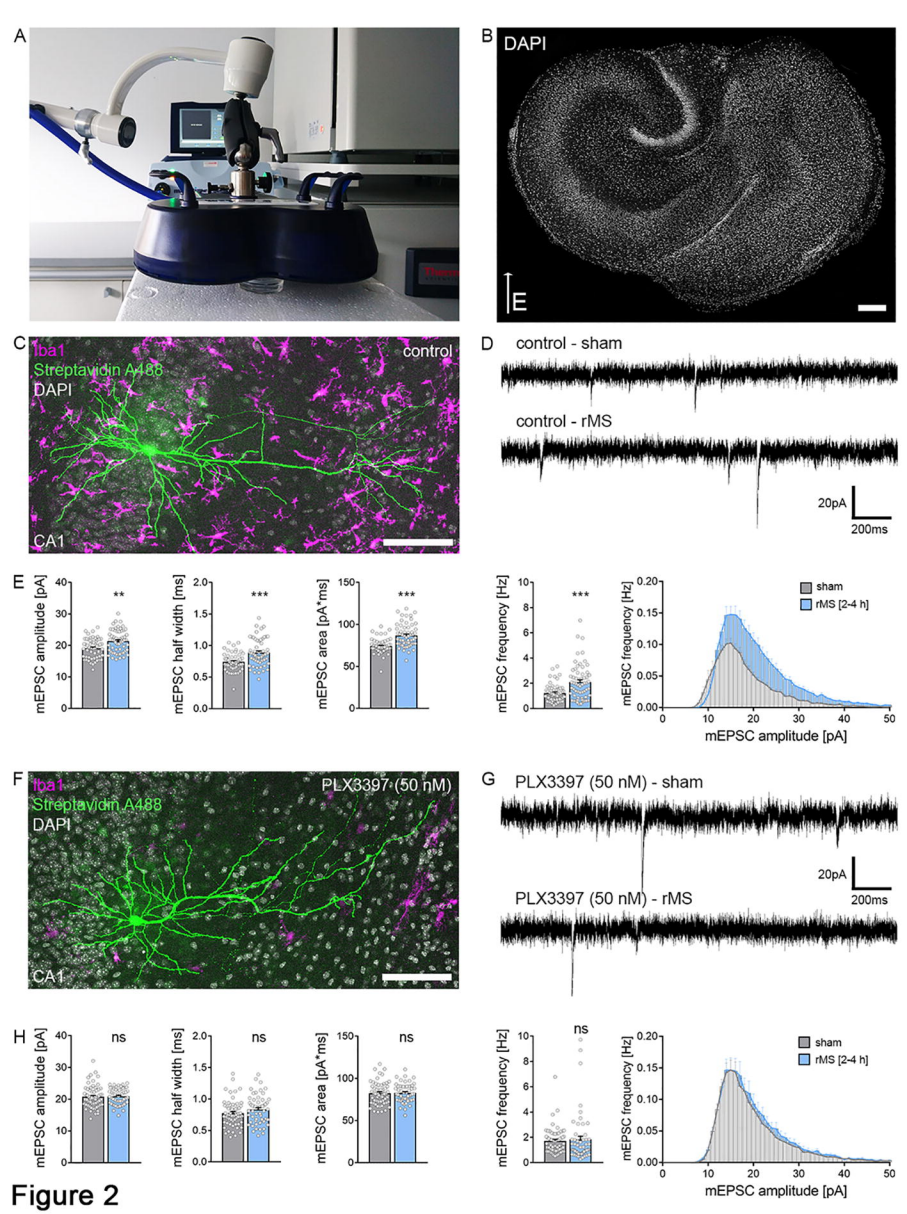
A
B
DAPI
E
C
Iba1
Streptavidin A488
DAPI
control
CA1
D
control - sham
control - rMS
20pA
200ms
E
mEPSC amplitude [pA]
mEPSC half width [ms]
mEPSC area [pA*ms]
mEPSC frequency [Hz]
**
***
***
***
sham
rMS [2-4 h]
mEPSC amplitude [pA]
F
Iba1
Streptavidin A488
DAPI
PLX3397 (50 nM)
CA1
G
PLX3397 (50 nM) - sham
PLX3397 (50 nM) - rMS
20pA
200ms
H
mEPSC amplitude [pA]
mEPSC half width [ms]
mEPSC area [pA*ms]
mEPSC frequency [Hz]
ns
ns
ns
ns
sham
rMS [2-4 h]
mEPSC amplitude [pA]

Figure 2

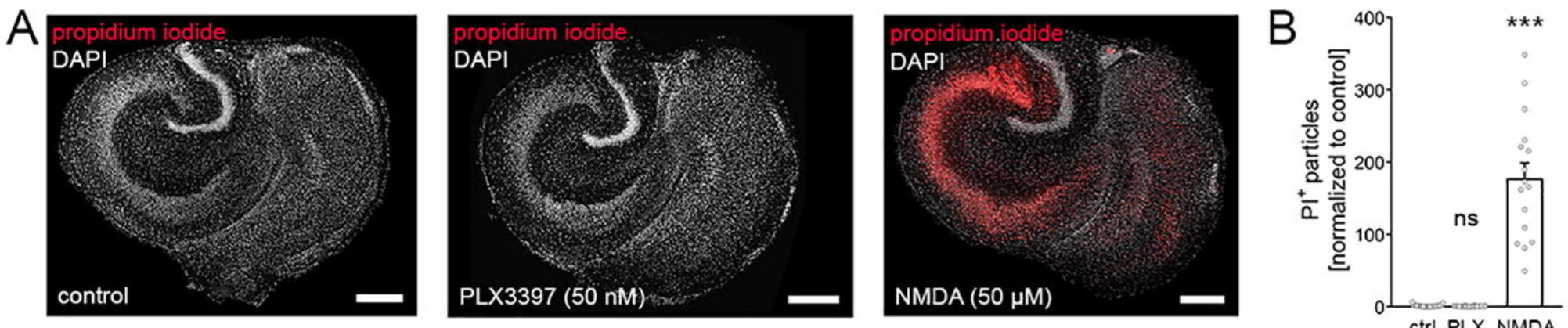
A
propidium iodide
DAPI
control
propidium iodide
DAPI
PLX3397 (50 nM)
propidium iodide
DAPI
NMDA (50 µM)
B
PI+ particles
[normalized to control]
400
300
200
100
0
***
ns
ctrl
PLX
NMDA

Figure 3

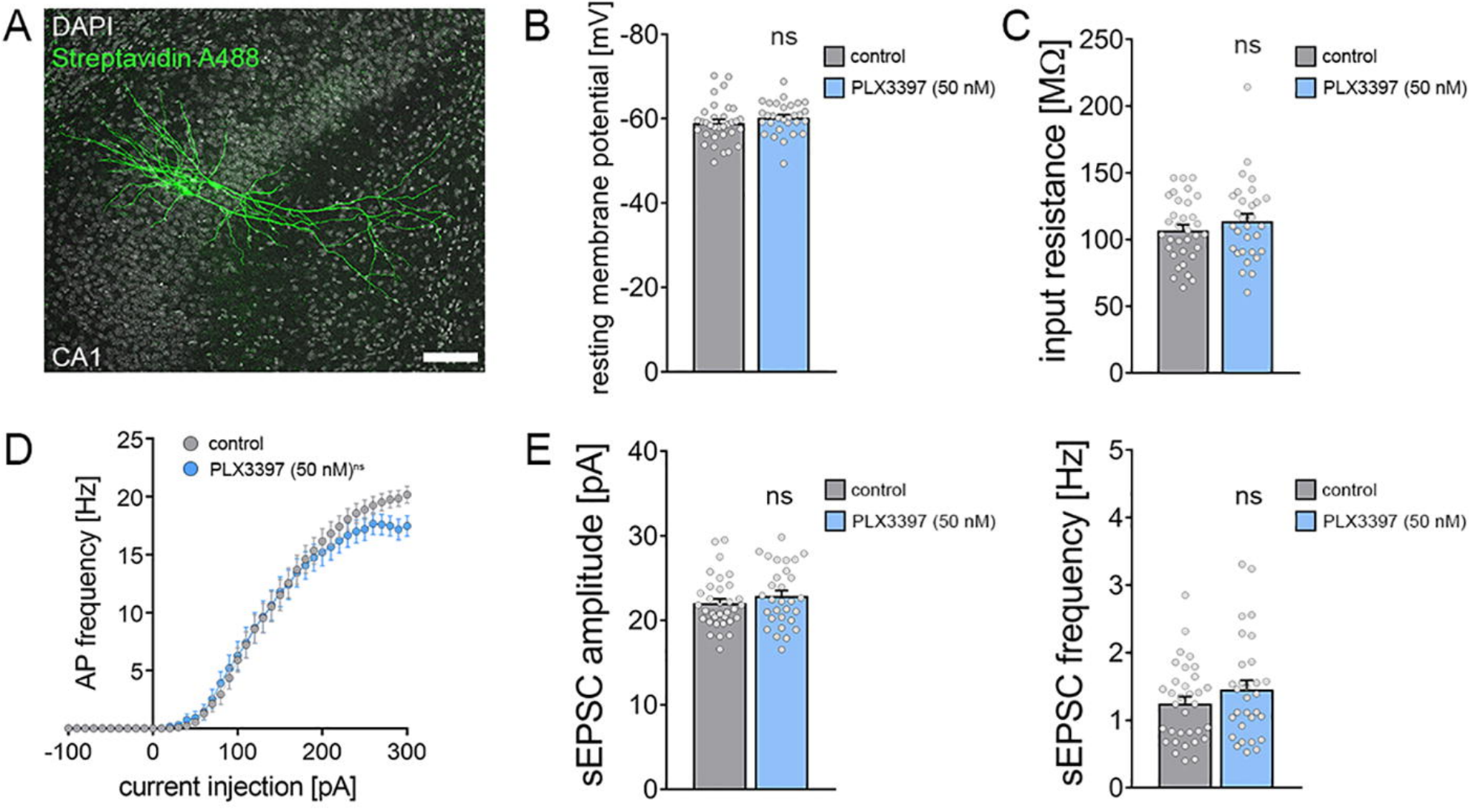
A
DAPI
Streptavidin A488
CA1
B
resting membrane potential [mV]
-80
-60
-40
-20
0
ns
control
PLX3397 (50 nM)
C
input resistance [MΩ]
250
200
150
100
50
0
ns
control
PLX3397 (50 nM)
D
AP frequency [Hz]
25
20
15
10
5
control
PLX3397 (50 nM)ns
-100
0
100
200
300
current injection [pA]
E
sEPSC amplitude [pA]
40
30
20
10
0
ns
control
PLX3397 (50 nM)
sEPSC frequency [Hz]
5
4
3
2
1
0
ns
control
PLX3397 (50 nM)

Figure 4

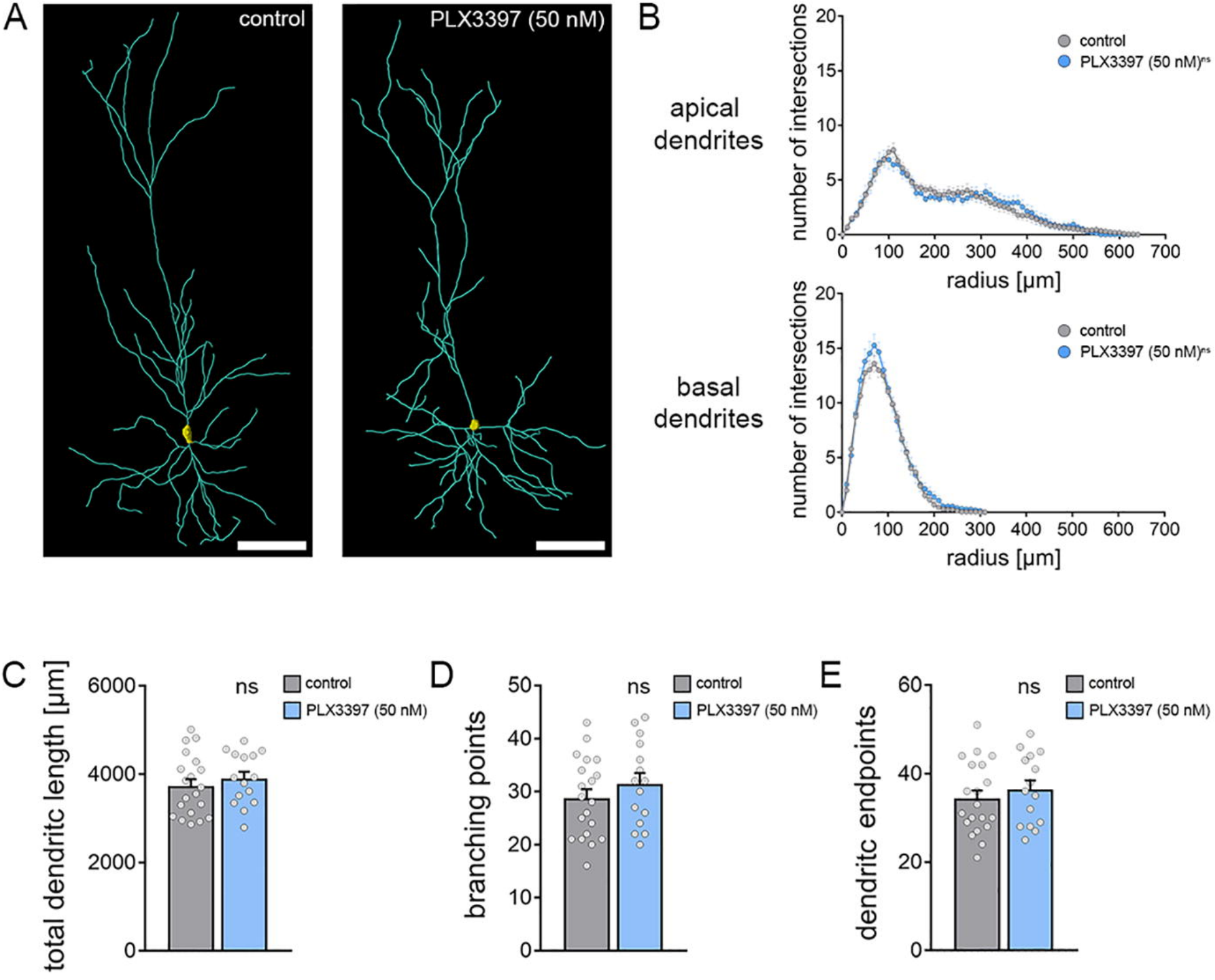
A
control
PLX3397 (50 nM)
B
apical dendrites
basal dendrites
number of intersections
radius [µm]
control
PLX3397 (50 nM)ns
C
total dendritc length [µm]
D
branching points
E
dendritc endpoints
ns

Figure 5

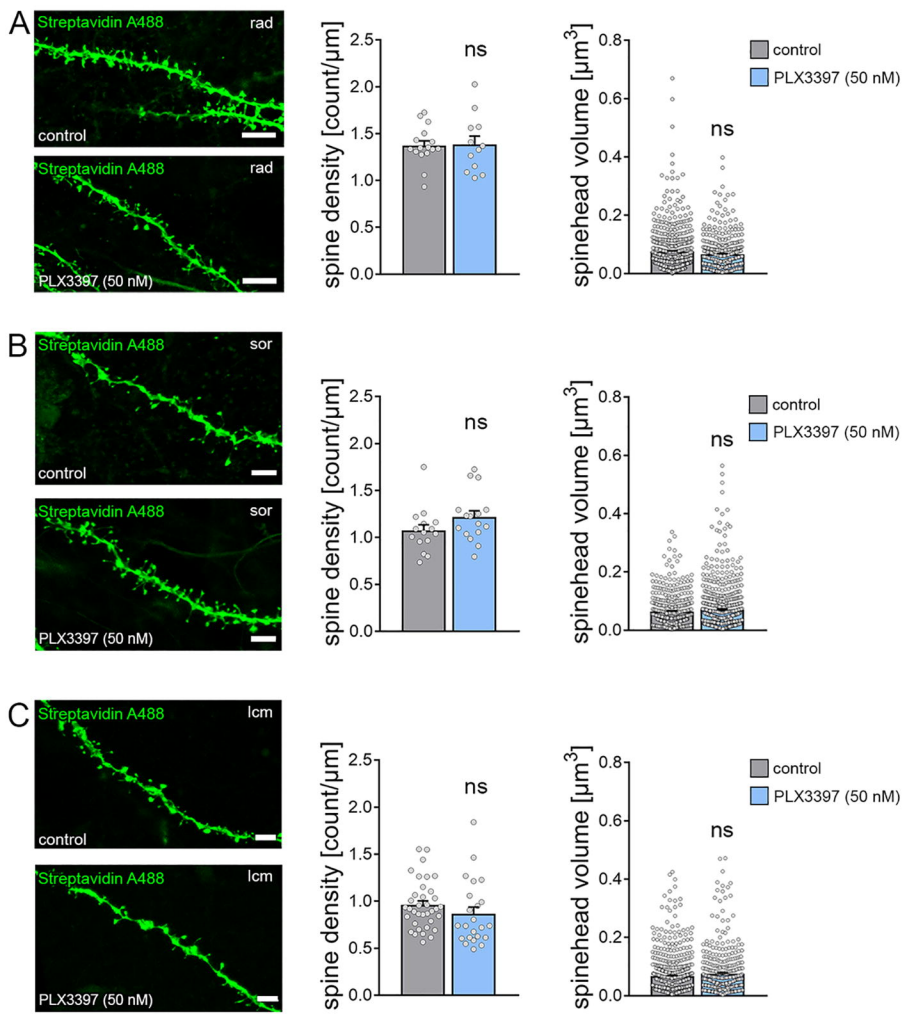
A
Streptavidin A488
rad
control
Streptavidin A488
rad
PLX3397 (50 nM)
spine density [count/µm]
ns
spinehead volume [µm3]
ns
control
PLX3397 (50 nM)
B
Streptavidin A488
sor
control
Streptavidin A488
sor
PLX3397 (50 nM)
spine density [count/µm]
ns
spinehead volume [µm3]
ns
control
PLX3397 (50 nM)
C
Streptavidin A488
lcm
control
Streptavidin A488
lcm
PLX3397 (50 nM)
spine density [count/µm]
ns
spinehead volume [µm3]
ns
control
PLX3397 (50 nM)

Figure 6

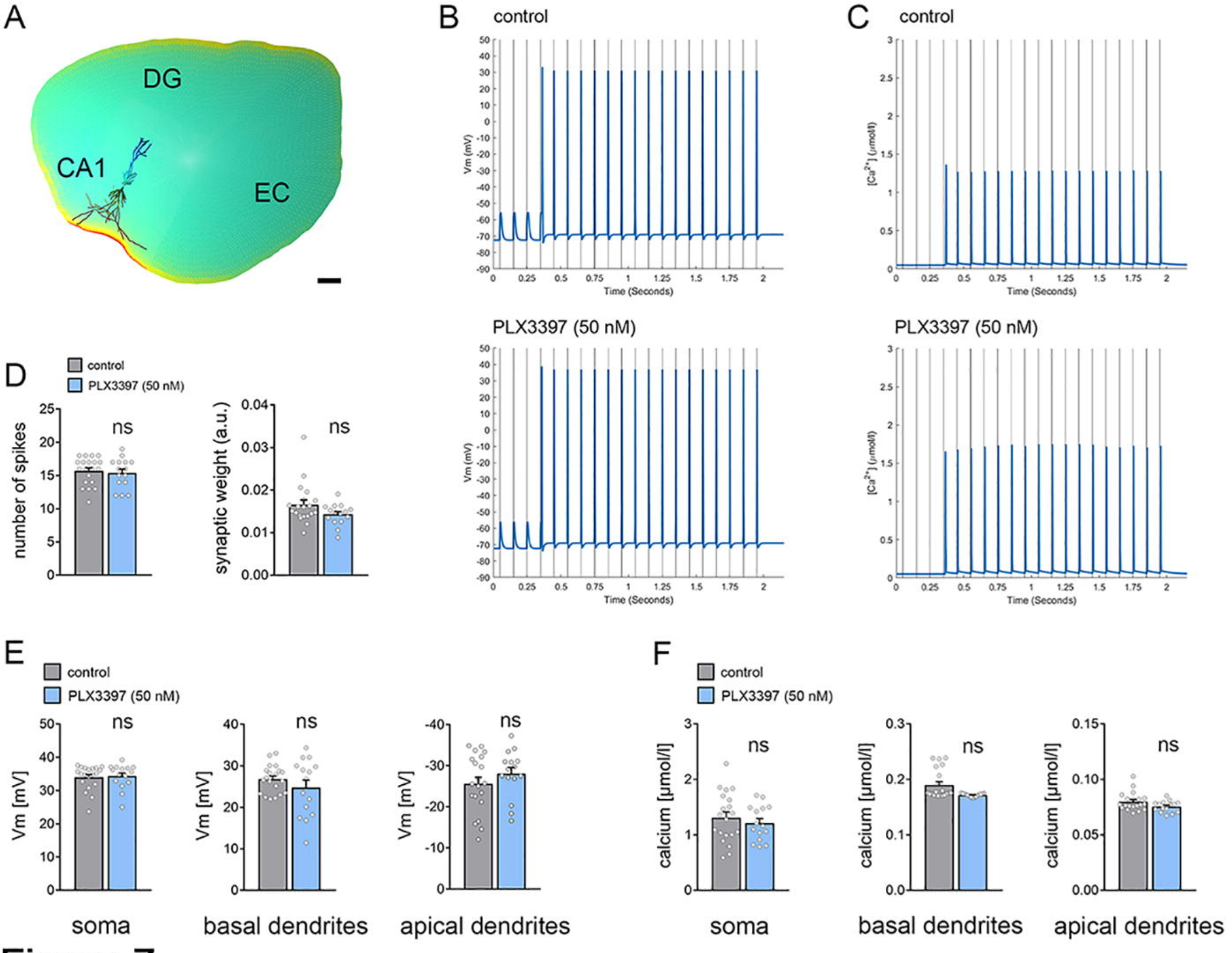
A
DG
CA1
EC
B
control
Vm (mV)
Time (Seconds)
PLX3397 (50 nM)
C
control
[Ca2+] (μmol/l)
Time (Seconds)
PLX3397 (50 nM)
D
control
PLX3397 (50 nM)
number of spikes
ns
synaptic weight (a.u.)
ns
E
control
PLX3397 (50 nM)
Vm [mV]
ns
soma
basal dendrites
apical dendrites
F
control
PLX3397 (50 nM)
calcium [μmol/l]
ns
soma
basal dendrites
apical dendrites

Figure 7

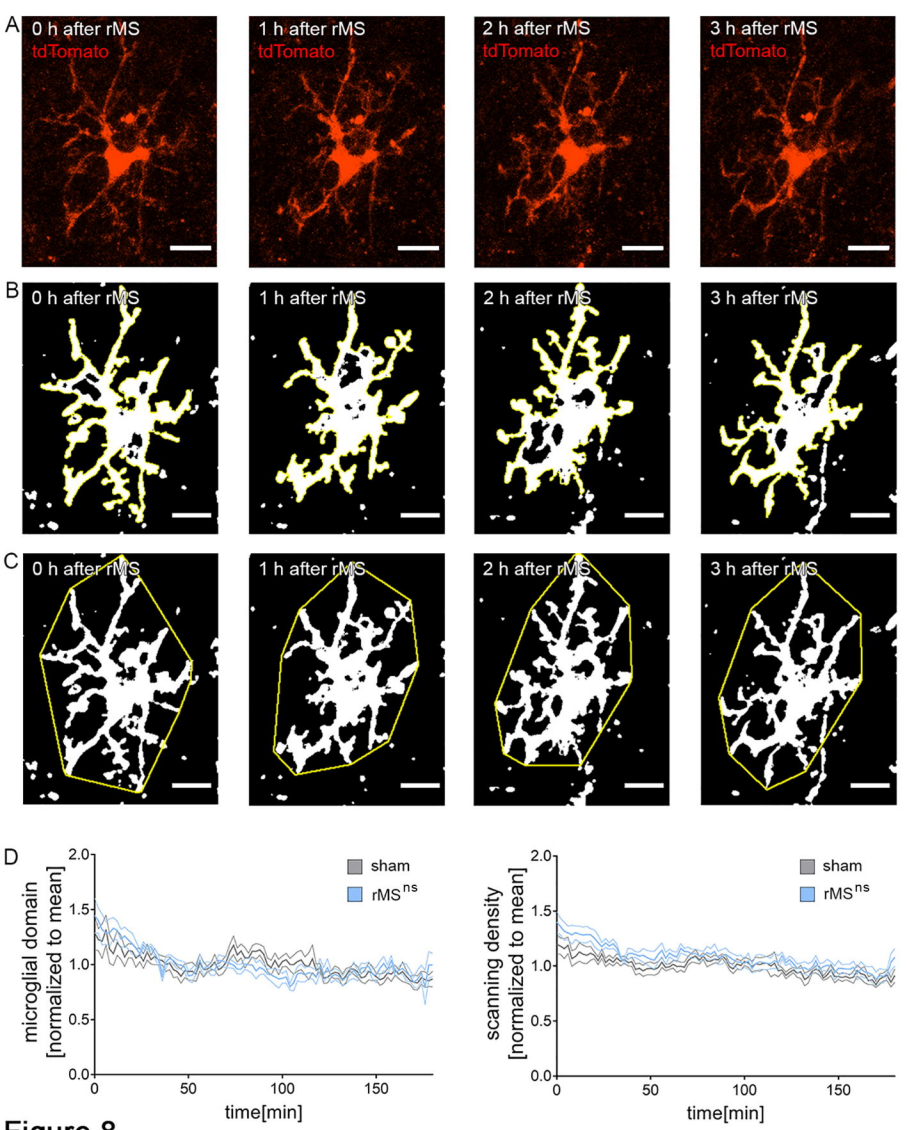
A
0 h after rMS
tdTomato
1 h after rMS
tdTomato
2 h after rMS
tdTomato
3 h after rMS
tdTomato
B
0 h after rMS
1 h after rMS
2 h after rMS
3 h after rMS
C
0 h after rMS
1 h after rMS
2 h after rMS
3 h after rMS
D
microglial domain
[normalized to mean]
sham
rMS ns
time[min]
scanning density
[normalized to mean]
sham
rMS ns
time[min]

Figure 8

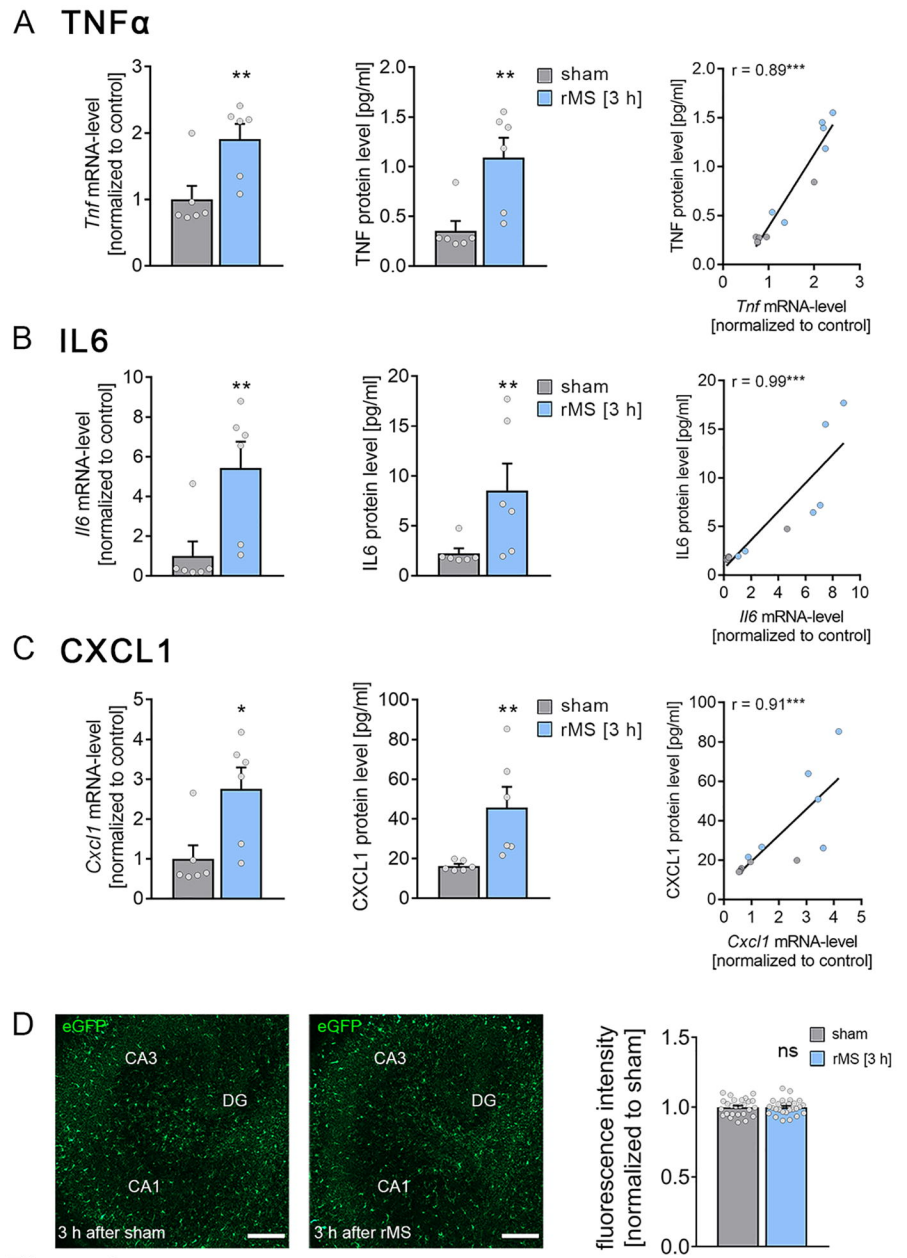
A TNFα
Tnf mRNA-level [normalized to control]
**
TNF protein level [pg/ml]
**
sham
rMS [3 h]
r = 0.89***
TNF protein level [pg/ml]
Tnf mRNA-level [normalized to control]
B IL6
Il6 mRNA-level [normalized to control]
**
IL6 protein level [pg/ml]
**
sham
rMS [3 h]
r = 0.99***
IL6 protein level [pg/ml]
Il6 mRNA-level [normalized to control]
C CXCL1
Cxcl1 mRNA-level [normalized to control]
*
CXCL1 protein level [pg/ml]
**
sham
rMS [3 h]
r = 0.91***
CXCL1 protein level [pg/ml]
Cxcl1 mRNA-level [normalized to control]
D
eGFP
CA3
DG
CA1
3 h after sham
eGFP
CA3
DG
CA1
3 h after rMS
fluorescence intensity [normalized to sham]
ns
sham
rMS [3 h]

Figure 9